Branching out of the Bighorn Basin: Records of Early Eocene Hyperthermals in the Piceance Basin of Western Colorado

A Senior Thesis
Presented to
The Faculty of the Department of Geology
The Colorado College

In Partial Fulfillment of the Requirements for the Degree
Bachelor of Arts

Fischer Hazen

May 2016

Acknowledgements

Table of Contents

List of Figures..

Abstract

The Eocene Thermal Maximum 2 (ETM2) and Hyperthermal 2 (H2) events are Paleogene hyperthermal events occurring ~53.7 mya and ~53.6 mya, respectively, and are characterized by increased global temperatures and an influx of isotopically light carbon to the exogenic carbon reservoir. Unlike the much better studied Paleocene Eocene Thermal Maximum (PETM), no descriptions of environmental change during these events have been published, and to date only one record of the ETM2 and H2 has been reported from terrestrial sections.

In this study, carbon isotope chemostratigraphy is used to identify records of the ETM2 and H2 in the Piceance Basin of western Colorado, and relate them to known section in the Bighorn Basin of Wyoming. Oxygen isotope records, weathering indices from major element concentrations in paleosols, and sedimentological changes are then used to study environmental and sedimentation changes associated with those events in the Piceance Basin. In particular, it is suggested that hyperthermal events are associated with a noted decrease in weathering intensity, decrease in soil moisture, enhanced seasonal precipitation, and a drastic change in the nature of sedimentation.

In the Piceance Basin, there is evidence for a decrease in weathering during the ETM2 event, a decrease in soil moisture, seasonal precipitation, and a drastic change in sedimentation flux. The importance of having a second terrestrial record of the ETM2 and H2 in the Piceance Basin is revealed through

comparison with the Bighorn Basin records. There are obvious geochemical and sedimentological differences between the two basins. Consequently, careful consideration must be applied when extrapolating environmental impacts from one locality through time or space in order to characterize the nature of terrestrial environmental change during hyperthermal events.

1) Introduction:

Earth's climate has been constantly evolving over the past 60 million years. Complex fluctuations in thermal regimes have resulted in extremes ranging from hothouse climates with ice-free poles to icehouse climates with expansive continental ice sheets. These climatic variations can take place gradually over millions of years driven by tectonic processes, they can be cyclic over 10s to 100s of thousands of years driven by orbital forcing, or they can be large, but brief, perturbations, on the scale of thousands of years (Zachos et al., 2001). Of particular interest are perturbations that took place during the Paleogene that are characterized by global increases in temperature, or hothouse climates, and are thus termed 'hyperthermal' events. They are associated with rapid changes to the near-surface carbon cycle (e.g, Zachos et al., 2008), in particular the addition of large amounts of carbon to atmospheric-ocean reservoirs (e.g, Bowen et al. 2006; Zachos et al., 2008; Abels et al., 2012), and as such they represent past analogs for present-day changes to the carbon cycle. Thus study of these events can advance understanding of how climate might change in the future, and what the impacts of such change may be in both marine and terrestrial environments.

The first and largest Paleogene hyperthermal event is the Paleocene - Eocene Thermal Maximum (PETM; also known as 'Eocene Thermal Maximum 1' or 'ETM1') which occurred ~56 Ma. It has been studied extensively at ~143 sites all over the world, in both marine and terrestrial environments (Figure 1) and

therefore a great deal is known about the likely causes of PETM warming and the impacts of this climate change (see review of PETM impacts in McInerny & Wing, 2011).

In contrast to the PETM, far less is known about later hyperthermal events, such as those occurring ~53.7 Ma (known as the ETM2 event) and ~53.6 Ma (known as the H2 event). The primary reason is that fewer records of these events are known to exist. Both the timing and development of these events are well constrained in marine records (Stap et al., 2010). However, these events are not well documented in terrestrial settings. Only the Bighorn Basin in Wyoming has a terrestrial sedimentological record that includes all three of the hyperthermal events (Abels et al., 2012), and to date, no descriptions of paleoenvironmental change during the ETM2 and H2 events have been described. This gap in knowledge is significant, and because of it we are not sure if the large PETM was a unique event characterized by distinctive causes and impacts, or whether all hyperthermal events share similar characteristics from place to place, even over a small region such as western North America.

The primary goals of this research are to (1) investigate & describe the impacts of ETM2 climate change in the Piceance Basin where a previously unpublished record of the event is identified, (2) compare our findings with those of ETM2 in the Bighorn Basin, and (3) develop a preliminary sedimentation model for the Piceance Basin. Comparison will allow for the identification of regional

rather than local impacts of change during ETM2, which will in turn allow for a

more robust comparison with records of change during the PETM.

2) Background

2.1) Paleocene Eocene Thermal Maximum (PETM)

The PETM is the most thoroughly studied hyperthermal event. Kennett and Stott (1991) published the first scientific literature focusing on a paired carbon isotope excursion (CIE) and oxygen isotope excursion in foraminiferal carbonate off the coast of Antarctica. This event later became the known as the PETM. Their findings included a rapid onset for the ~6 Ka excursion, a negative shift in oxygen isotope ratios ($\delta^{18}O$) and in carbon isotope ratios ($\delta^{13}C$), which were synchronous with an extinction of benthic foraminifera (Thomas, 1989). The negative CIE was then discovered in pedogenic carbonate and mammalian tooth enamel from continental sources (Koch et al., 1992), indicating that PETM was a global event that was preserved within both continental and oceanic sections.

Recent estimates for the age of the PETM onset, through radiometric dating of marine ash layers and orbital turning of marine sediment, are 56.021 – 56.293 Ma (Westerhold et al., 2009). The duration of the PETM has been estimated to be between from 150–220 Ka to 120–220 Ka in oceanic sections using astronomical cyclostratigraphy and extraterrestrial He^3 fluxes (McInerny and Wing, 2011). These values are corroborated from continental PETM sections where estimated duration is ~157 Ka (Aziz et al., 2008). Stable isotope data indicate the negative shift in $\delta^{13}C$ for the PETM CIE had a magnitude of approximately -4.7‰ ± 1.5‰ in terrestrial records and -2.8‰ ± 1.3‰ for marine records (McInerny and Wing, 2011).

Environmental changes during the PETM are numerous and include shifts in temperature, precipitation, and climatic patterns. An approximate 5 °C temperature increase in deep-water temperature (Zachos et al., 2001) was inferred from the negative $\delta^{18}O$ excursion. This ~5-7 °C temperature increase was also observed in the Bighorn Basin, Wyoming via the study of paleobotany, $\delta^{18}O$ of fish scales, $\delta^{18}O$ of tooth enamel, and clumped isotopes of soil nodules (McInerny and Wing, 2011; Snell et al., 2013). Similar polar temperature increases of ~5-8 °C temperature were estimated using biomarker thermometry (TEX_{86}) (Sluijs et al., 2006).

In addition to the global temperature increase during the PETM, there is also significant evidence for changes in runoff, and by extension, continental precipitation patterns. Increased abundances of kaolinite, combined with a noted increase in eutrophic dinoflagellate populations in coastal strata, has pointed to increased runoff and erosion during the PETM. Given the relationship between sediment production and precipitation, and the fact that the highest sediment production values occur in seasonal precipitation climates, climate patterns during the PETM are hypothesized to have been more seasonal and episodic in contrast to non-hyperthermal intervals (McInerny and Wing, 2011).

Increased seasonality in precipitation on a global scale is supported by a range of sedimentological studies from a range of marine and terrestrial sites. These included the identification of mega-fan conglomerate units indicative of intense and sporadic precipitation in Spain (Schmitz and Pujalte, 2007). Marine

deposits in Austria indicate an increase in siliciclastic deposition consistent with an increase in seasonal precipitation (Egger et al., 2005). Paleosols in North America indicate less chemical weathering (Kraus and Riggins, 2007), and a decrease in leaf size signifies an increase in water stress (Wing et al., 2009). These studies are consistent with an increase in seasonal and variable precipitation on a global scale for the PETM.

The PETM is commonly associated with, and thought to be the result of, a large release of isotopically light carbon into both the atmosphere and oceans. However, the mechanism and the source of the $\delta^{13}C$ depleted carbon is widely debated. Proposed sources include (1) destabilization of methane clathrates (Dickens et al., 1997), (2) wildfires (Moore and Kurtz, 2008), (3) thermogenic methane release (Westerhold et al., 2009), (4) drying epicontinental seas (Higgins and Schrag, 2006) and (5) melting permafrost (DeConto et al., 2010).

Some of the greatest impacts of the PETM are noted below. Macrofossils from more than 50 ocean cores and outcrops, ranging from the poles to equatorial regions and in all of the major oceanic basins of the world (Figure 1), indicate that the PETM records the largest benthic foraminiferal extinction in the past 90 myr. Over 30-50% of the species went extinct, and this event is referred to as the benthic foram extinction. It is one of only three major overturns in benthic foram fauna since the middle Mesozoic (Thomas, 2007; McInerny and Wing, 2011).

Terrestrial fossils and biomarkers from a multitude of localities (Figure 1), primarily northern hemisphere in the equatorial region, demonstrate that there was a rapid radiation of mammalian species at the onset of the PETM CIE. This event is sometimes referred to as the mammalian dispersal event, and is thought to be the result of mammalian migration across high altitude land bridges during the hothouse climate (Hooker, 1998).

Figure 1) PETM Study Localities
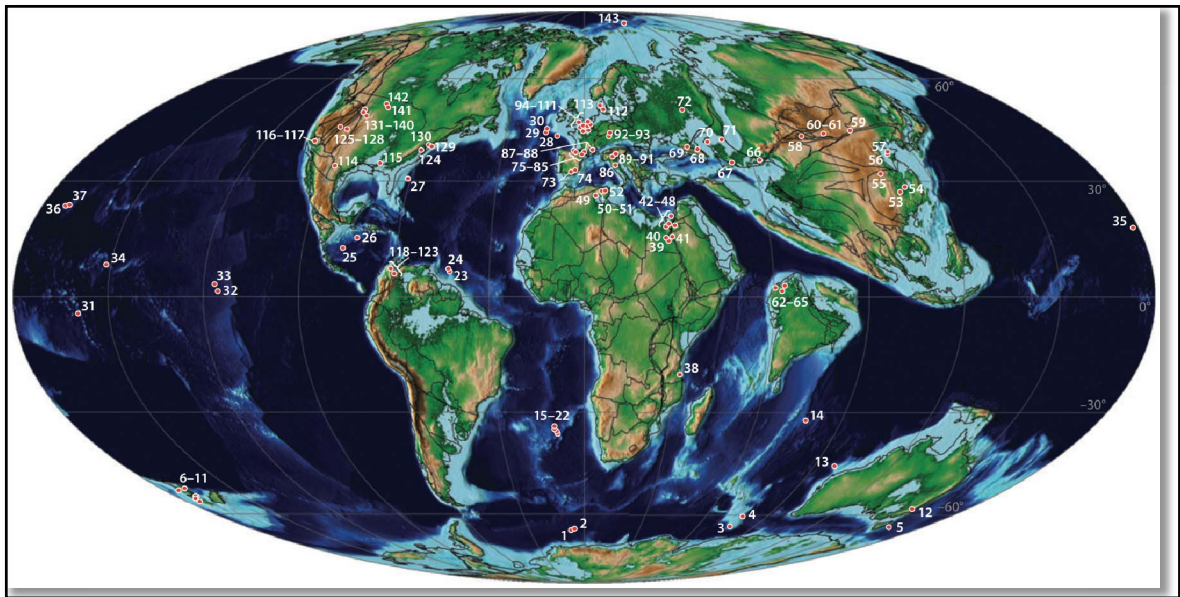
This global paleogeographical map (~56 Ma) depicts both marine and terrestrial PETM study locations. Black lines indicate plate boundaries and colors indicate elevation and bathymetric depth. Numbers indicate PETM study sites and tie in with Supplemental Table 1 at the following link: http://www.annualreviews.org/doi/suppl/10.1146/annurev-earth-040610-133431 (McInerny and Wing, 2011)

2.2) Eocene Thermal Maximum 2 (ETM2 or H1)

Due to the small number of both terrestrial (n=1) and marine (n=3) records of the ETM2 event, it is less well known than the PETM. Marine carbon and oxygen isotope records constrain both the timing and development of this event, but, there are only six total sections from three sites (Figure 2), four from a transect along Walvis Ridge, Atlantic Ocean, one from Maud Rise, Weddell Sea (Stap et al., 2010), and one from the Lomonosov Ridge, Artic Ocean (Sluijs et al., 2009; Krishnan et al., 2014).

To date, only one terrestrial record of ETM2 is known and that is from the Bighorn Basin in Wyoming (Abels et al., 2012). It is located in the Wasatchian 5 faunal biozone (Abels et al., 2012), and is dated to 53.7 Ma (Lourens et al., 2005). The associated CIE has been measured at -1.0‰ – -1.5‰ in oceanic carbonate and ~ -3.5‰ in bulk organic matter. It resulted in a ~3 °C oceanic temperature increase (Lourens et al., 2005, Stap et al., 2010). These measured values are approximately half of what has been interpreted for the PETM. This isotopic change is mirrored by increased development of channel sandstone complexes and large mud filled scours during the ETM2 – H2 interval (Abels et al., 2012). In the Bighorn Basin section, no paleoenvironmental interpretations associated with ETM2 have been published.

Figure 2) ETM2 Marine Study Localities
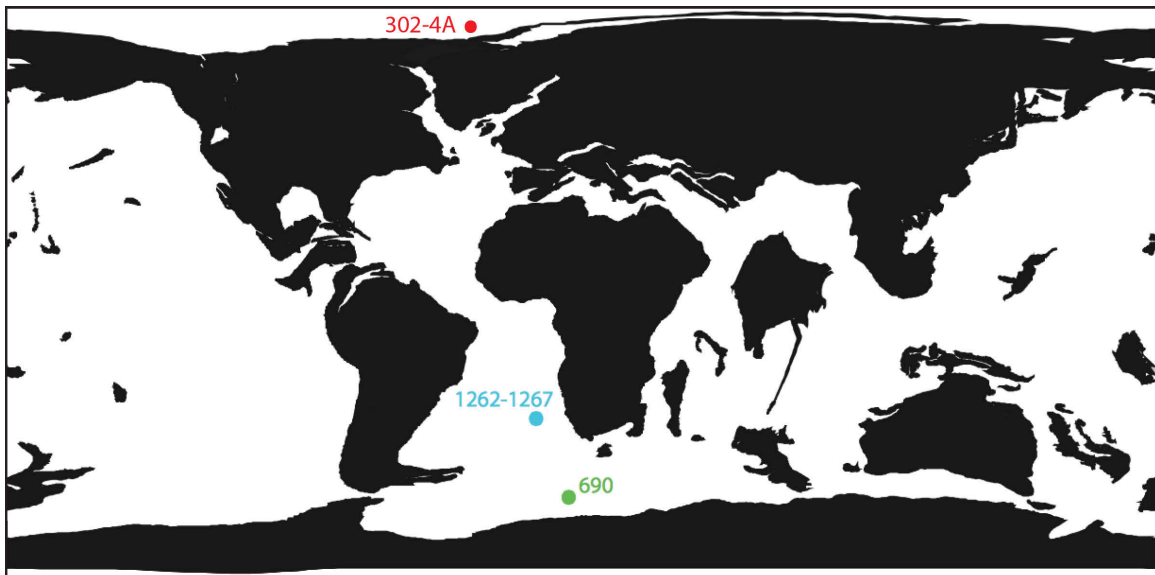
This global map demarcates the six marine sample sites with records of ETM2 and H2. Sites 1262 to 1267 are the four sample sites on the Walvis Ridge and site 690 is located in the Maud Rise. Site 302-4A is the site from the Lomonosov Ridge, Artic Ocean (Sluijs et al.) This figure is located in in the 2010 GSA Data Repository; item 2010166, figure DR1. It is available at the following link: ftp://rock.geosociety.org/pub/reposit/2010/2010166.pdf (Stap et al. 2010) The Lomonosov Ridge data point was added secondarily.

2.3) Paleosol and Carbonate Nodule Formation

Paleosols are defined as soils that formed on past landscapes and have since been preserved in the rock record (Mack et al., 1993). They initiate as overbank avulsion deposits on floodplains that then undergo weathering, leeching, and movement of ions, eventually forming distinct soil horizons (Abels et al., 2012). During seasonally wet periods, ions are leeched from the O (organic), A (surface), and E (eluvial) soil horizons and transported down into the B (subsoil) horizon where the ions then precipitate out during dry periods, or as the groundwater becomes supersaturated. It is important to recognize that paleosol formation requires episodic sedimentation followed by seasonal weathering, allowing for soil horizon development (Kraus, 1997).

Soil formation, and therefore paleosol formation, is controlled by a multitude of factors including (1) amount of seasonal precipitation, (2) soil temperature, (3) soil pH, (4) soil redox conditions, (5) cation exchange capacity, and (6) bulk soil density (Mack et al., 1993). As any of these factors change, the resulting soil formed reflects the change in formation parameters. Consequently the study of paleosols can provide insight into the conditions of formation for the studied paleosol.

Carbonate nodules, representing authigenic carbonate, are integral to the study and understanding of paleoclimate, especially within the field of stable isotope geochemistry. These nodules form in place and are primarily composed of calcite ($CaCO_3$), but also include a handful of trace elements that substitute for

calcium during formation. Carbonate nodules typically form in subhumid to arid regions that experience seasonal climate and precipitation trends (Breeker et al., 2009). Nodule formation is a complex process requiring seasonal variability including a wet and a dry season within a soil.

During the wet season, chemical and physical weathering of source material, results in the dissolution of Ca^{2+} and other ions into the surface and ground water reservoirs. These ions are transported through the O, A and E soil horizons and into the B_k horizon. Simultaneously, CO_2 dissolves into the groundwater and carbonic acid is produced (Equation 1).

$$H_2O + CO_2 = H_2CO_3 \hspace{4cm} (1)$$

$$CaCO_3 + H_2CO_3 = Ca^{+2} + 2HCO_3^- \hspace{2.5cm} (2)$$

$$CaCO_3 + H_2O + CO_2 = Ca^{+2} + 2HCO_3^- \hspace{1.8cm} (3) = (1) + (2)$$
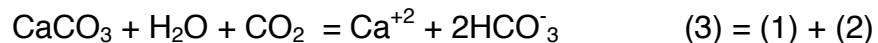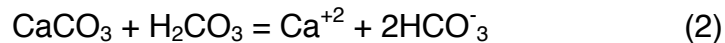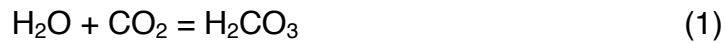
Equations 1, 2 and 3
_____

Equation 1 shows the formation of carbonic acid (H_2CO_3) as Carbon Dioxide (CO_2) dissolves into the groundwater. Equation 2 shows the relationship between Calcite ($CaCO_3$), Carbonic Acid (H_2CO_3), Calcium (Ca^{2+}) and a byproduct Bicarbonate (HCO_3^-). Equation 3 is the combination of Equations 1 and 2. Calcite precipitation is influenced by the pCO_2 of soils and the presence of Ca^{2+}.

CO$_2$ is introduced to the soils by autotrophic respiration through plant roots or heterotrophic respiration through microbial oxidation of organic matter. Both processes combined are referred to as soil respiration (Breeker et al., 2009; Cerling, 1984). The isotopic concentration of carbon within the CO$_2$ produced via soil respiration ($\delta^{13}C_r$) is very low as a result of a double carbon fractionation as CO$_2$ moves through the cell wall and is then fixed by Rubisco. $\delta^{13}C_r$ then mixes with atmospheric CO$_2$, resulting in soil CO$_2$ with a new isotopic concentration of soil carbon ($\delta^{13}C_s$) that falls somewhere between -7.0 ‰ and -11.0 ‰ during non-hyperthermal periods for paleosols that were covered by C3 vegetation (Abels et al., 2012; Abels et al., 2015).

Oxygen isotopic concentration in soils ($\delta^{18}O_s$) is primarily a function of the $\delta^{18}O$ of precipitation and subsequent effects of evapotranspiration. As moisture travels across the continent, Rayleigh Distillation occurs resulting in the preferential rain out of ^{18}O with distance from the source; cold temperatures or elevation gains magnify this effect. Evapotranspiration, once the water is in the soils, has the opposite effect. ^{16}O is preferentially evaporated at a rate dependent on the overlying atmospheric humidity, resulting in water generally enriched in ^{18}O (Breeker et al., 2009).

During the dry season, increased temperatures and drier conditions result in (1) supersaturation of Ca^{2+} as water is removed from soils through evapotranspiration (2) decreased plant activity because less water results in lower pCO$_2$, and (3) increased soil temperatures. These three factors result in

increased carbonate precipitation (Equation 3, 4) (Breeker et al., 2009). As nodule formation only occurs in dry seasons, the $\delta^{18}O$ ratios only reflect summer or dry season isotopic values due to the temperature dependent fractionation that occurs with the formation of carbonate. These processes are described by equations 1, 2, 3 and 4.

$$a_{CaCO_3} = \frac{4m^3_{Ca^{2+}}}{pCO_2}\left(\frac{K_2}{K_1 K_{cal} K_{CO_2}}\right) \qquad (4)$$

Equation 4

Equation 4 demonstrates that the rate at which calcite precipitates is a function of Ca^{2+} concentration (m_{Ca2+}), the partial pressure of CO_2 (pCO_2) and dissociation constants for carbonic acid, bicarbonate and calcite (K_1, K_2, K_{cal} respectively) (Breeker et al., 2009)

3) Geological Setting & Sample Collection

3.1) Piceance Creek Basin

The Piceance Creek Basin is an intermontaine basin located approximately 30 miles north east of Grand Junction, CO near De Beque, CO (Figure 3). The Piceance Creek Basin is 100 miles long and 40–50 miles wide, with the long axis of the basin oriented northwest southeast. This basin is one of many sedimentologically isolated terrestrial basins produced during the Laramide Orogeny and associated uplift (Dickinson et al., 1988). It served as a sediment trap during the Laramide Orogeny, and contains a variety of Cretaceous through Eocene geologic formations (Figure 4).

The older Paleogene rocks are the Ohio Creek Formation and the Atwell Gulch Formation. The latter of which is a highly variable unit that overlies the massive sandstone of the Ohio Creek Formation. The base of the Atwell Gulch Formation contains a lignite layer and carbonaceous shale, which is overlain by 200 feet of gray siltstone and claystone, and another 150 feet of lenticular brown sandstone, carbonaceous shale and lignite beds on top of that (Donnell, 1969).

The fairly sharp and delineated contact between the Atwell Gulch Formation and the overlying Molina Formation is at the base of a prominent and mostly continuous arkosic sandstone bed. The Molina Formation consists of regular, continuous, thick-bedded, arkosic, brown/tan sandstone beds. There is some variation in color with some localized zones of red, green or grey sandstone beds. Minor amounts of clay separate the sandstone beds (Donnell,

1969). Recent chemostratigraphic work has suggested that the PETM is identified within the Molina Formation (Foreman et al, 2012).

The Shire Member (Figure 5) sits above the Molina Formation and below the Green River Formation. The Shire Member primarily consists of interbedded lenticular, non-continuous, sandstone beds and purple, red, orange and tan paleosol units (Donnell, 1969). Biostratigraphy indicates that the Shire is early Eocene in age, with fossils of Wasatchian land mammal ages 2 through 6 (Burger, personal communication, 2015).

To the northwest of our field area, fluvial rocks and the Shire Member interfinger with lake deposits. The lakes formed in the early Eocene and eventually joined with lake Uintah during the Long Point transgression in the Eocene (Johnson, 2012). The upper contact between the Shire and the Green River is at the base of the lowermost, prominent sandstone bed of the Green River Formation. The Green River is an oil rich and carbonaceous shale unit deposited in Lake Uintah in the Piceance Basin.

Figure 3) Location Map of Study Area
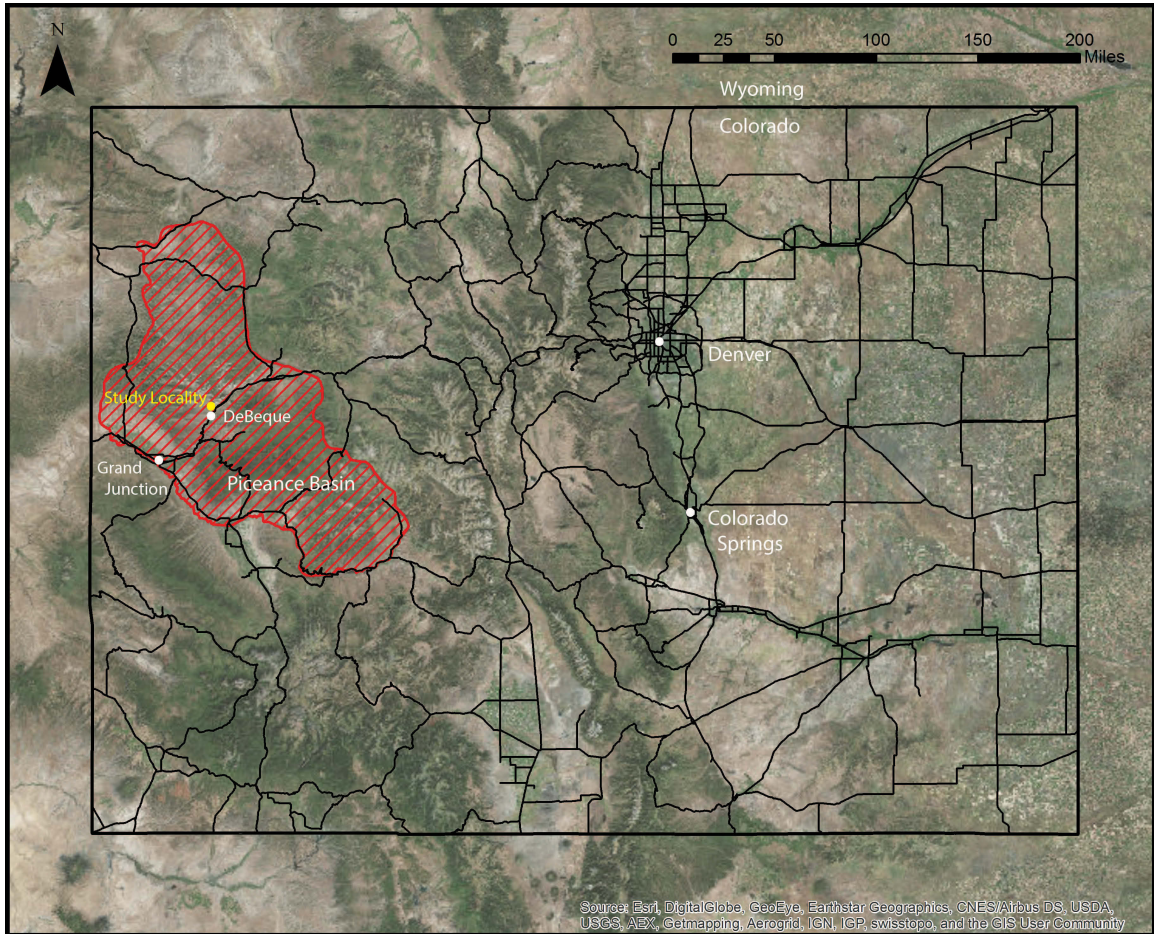
The Piceance Creek Basin, located in western Colorado, is highlighted in red. Major cities are highlighted in white and major roads are shown in black. The study locality is located ~10 miles west of De Beque and is highlighted in yellow. Piceance Basin boundary from USGS GIS data.

Figure 4) Geologic Map of Piceance Basin
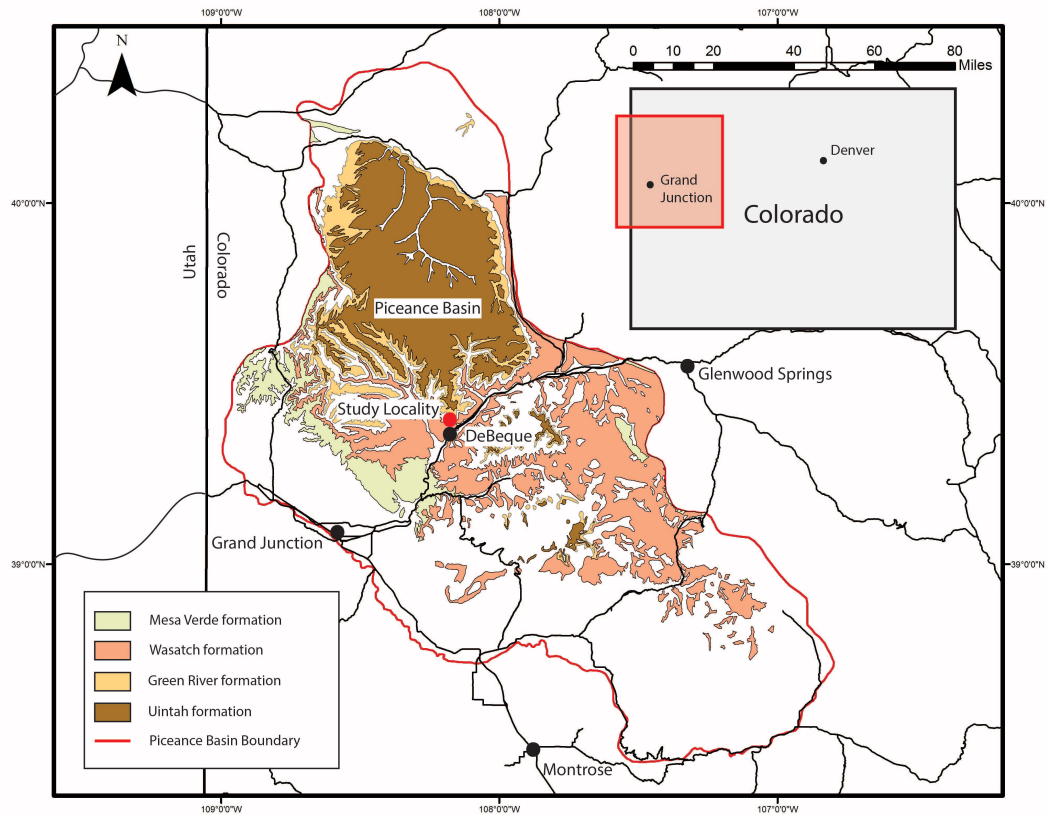
Geologic map of northwestern Colorado highlights outcrops of the Cretaceous Mesaverde Formation [green], the Eocene Wasatch formation [red], the Green River formation [tan] and the Uinta formation [brown] in the Piceance Basin. Geologic units and Piceance Basin boundary from USGS GIS data.

Figure 5) Image of Study Area

50 M
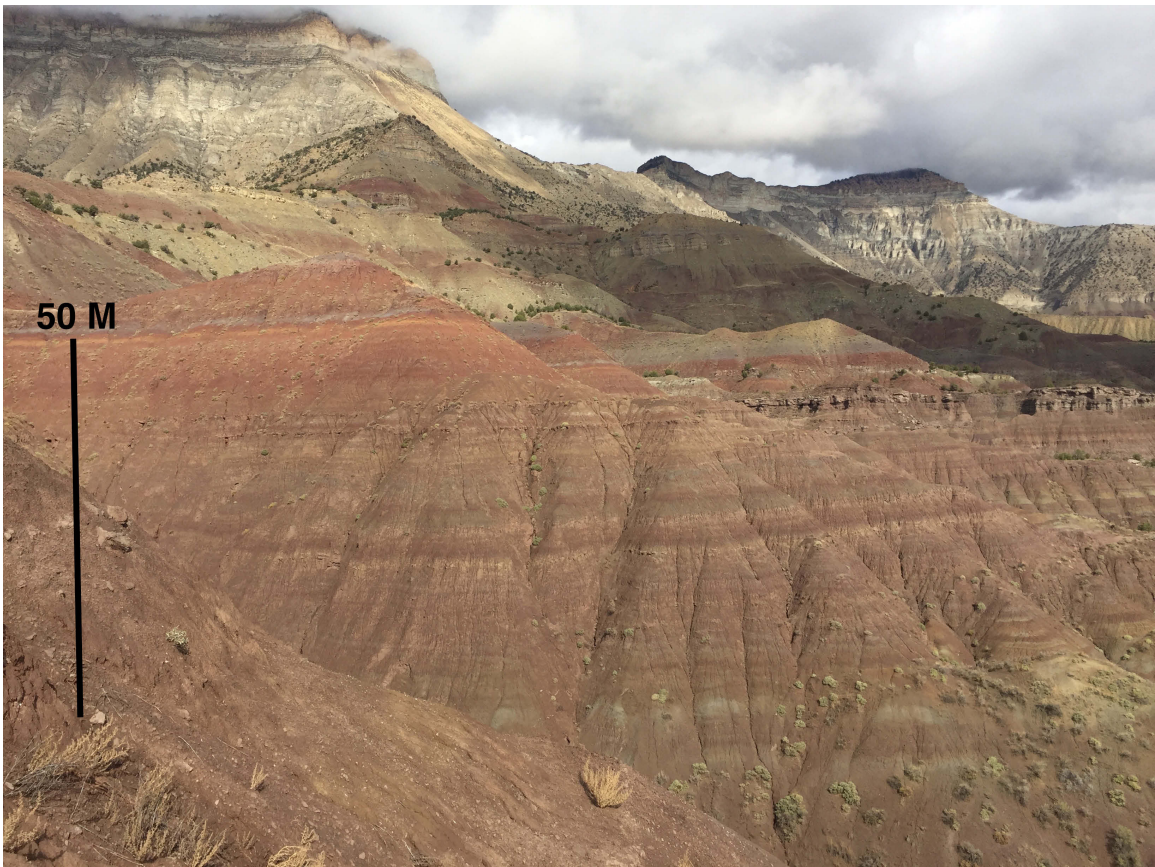
The above image is taken to the northeast and depicts the Shire member of the Wasatch formation in the Piceance Basin. The banded paleosols seen in the middle of the image are those on which this study focused.

3.2) Sample Collection

Within the Piceance Basin, morphologic features of paleosols, including color, qualitative grain size, bed thickness and spatial relationships with sandstone bodies were recorded in the field. Further fieldwork included sample collection of a 1–2 meter spaced suite of paleosol carbonate nodules and associated paleosol matrix from the study locality (Figure 3, Figure 4)**.** Specifically, 53 levels were sampled for carbonate nodules and associated paleosol matrix from a 91.73 meter stratigraphic section (Figure 5).

Two nodules from each level were selected and cut in preparation for chemical analysis. Milligram-sized samples of carbonate were taken for stable isotope analysis using a Dremel drill with diamond-tipped bits.

Paleosol samples were powdered and decalcified to remove secondary carbonate contamination using 0.1 M HCL. Each sample was mixed with HCL until off-gassing stopped. Samples were then washed three times with deionized water and spun in a centrifuge following each wash cycle. All decalcified samples were dried at 100 °C for a minimum of 12 hours and re-powdered. In preparation for XRF analysis, decalcified sample powders were then weighed to 1.1000 ± .0005 g and combined with 11.0000 ± .0010 g of anhydrous Lithium Borate Flux. The samples were melted, agitated and then fused in platinum crucibles at 1065 °C for 15 minutes in a Claisse LeNeo Fluxer.

4) Methods and Results:

4.1) Carbon and Oxygen Isotopes

Stable isotope ratios are reported as $\delta^{13}C$ and $\delta^{18}O$, where $\delta = (R_{sample}/R_{standard} - 1)*1000$ ‰. The standard is VPDB for carbon and VSMOW for oxygen. $\delta^{13}C$ and $\delta^{18}O$ of carbonate were measured using an automated carbonate preparation device (KIEL-III) coupled to a Finnigan MAT 252 isotope ratio mass spectrometer at the University of Arizona. Powdered samples were reacted with dehydrated phosphoric acid under vacuum at 70°C in the presence of silver foil. The isotope ratio measurement is calibrated based on repeated measurements of NBS-19, NBS-18, and in-house powdered carbonate standards. Analytical precision is ± 0.1 ‰ for both $\delta^{18}O$ and $\delta^{13}C$ (1s). The carbonate – CO_2 fractionation for the acid extraction is assumed to be identical to calcite. Isotope data from the Bighorn Basin was obtained from Abels et al. 2015. Results presented in Table 1.

4.2) Major Element Data

Samples were analyzed in the PANalytical Epsilon5 XRF at Colorado College to determine major oxide weight percent within paleosol clay minerals for soil weathering analysis. Analytical precision is ± 0.172 % for all major element data. Results are presented in Table 2 and Table 3. Rather than present all data, selected ratios of major elements are given. In particular, these ratios are used: (1) CALMAG [$Al_2O_3/(Al_2O_3 + CaO + MgO$) x 100], (2) Al/Si, (3)

(Ca+K+Mg+Na)/Al, (4) Ca/Al, (5) K/Al, (6) Mg/Al (Nordt and Driesse, 2010), and

(7) Fe and Mn values (Sheldon and Tabor, 2009).

4.3) Geochemical Data vs. Stratigraphic Position

All data is plotted vs. stratigraphic position and compared to the Bighorn

Basin record (Figure 6). Details of this figure are discussed in detail below.

Figure 6) δ¹³C, δ¹⁸O and CALMAG comparison for PB and BHB
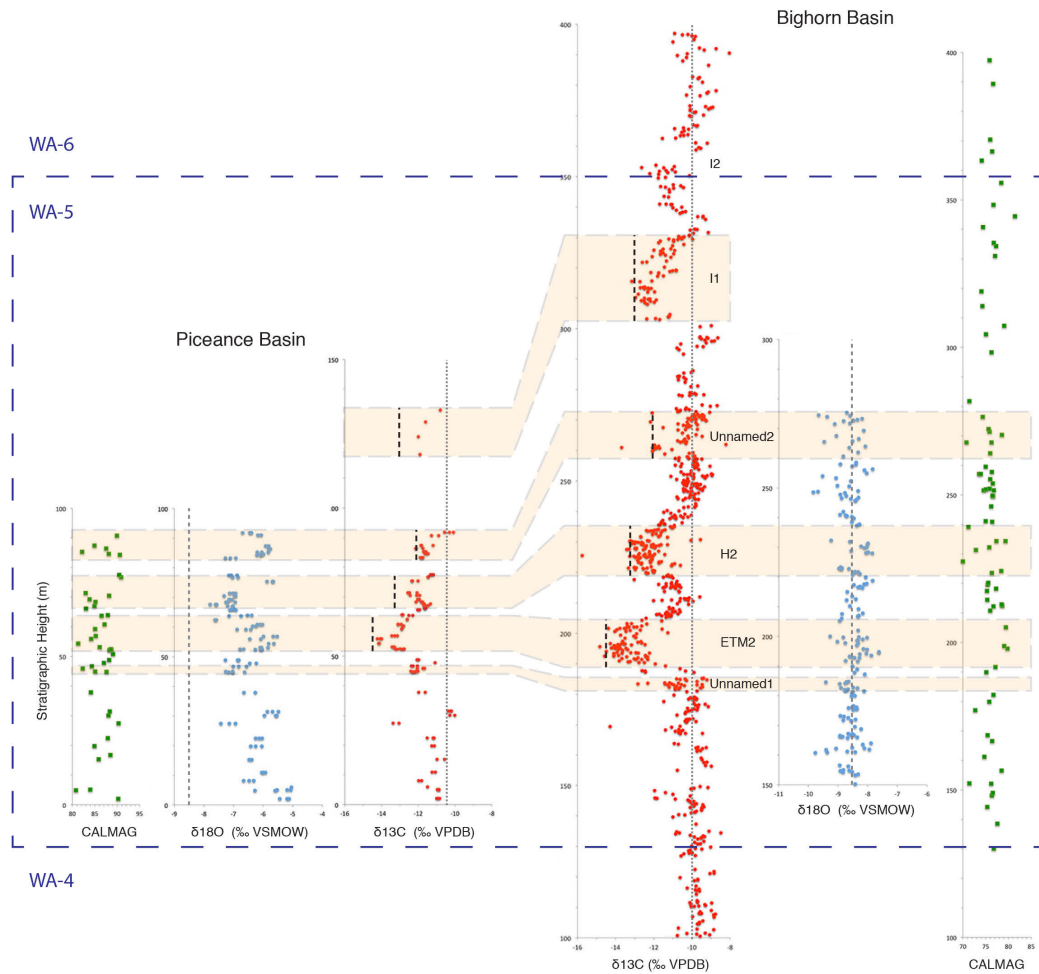
Carbon isotope, oxygen isotope and CALMAG curves are plotted from both the Piceance Basin and the Bighorn Basin. The three Bighorn Basin curves are plotted to the right (Abels et al., 2015). Wasatchian faunal zones are outlined in purple. Tan bars delineate interpreted chemostratigraphic correlations between the named hyperthermals in the Bighorn Basin and the newly discovered hyperthermals in the Piceance Basin. Bars are stretched to incorporate both the oxygen isotope and CALMAG data in order to better constrain trends in data for hyperthermal events. CALMAG regressions from Nordt and Driesse (2009), all oxygen isotope data plotted against SMOW and all carbon isotope data plotted against PDB. Data for Piceance Basin is located in Table 1 and Table 2.

33

Figure 7) δ¹³C comparison for PB and BHB
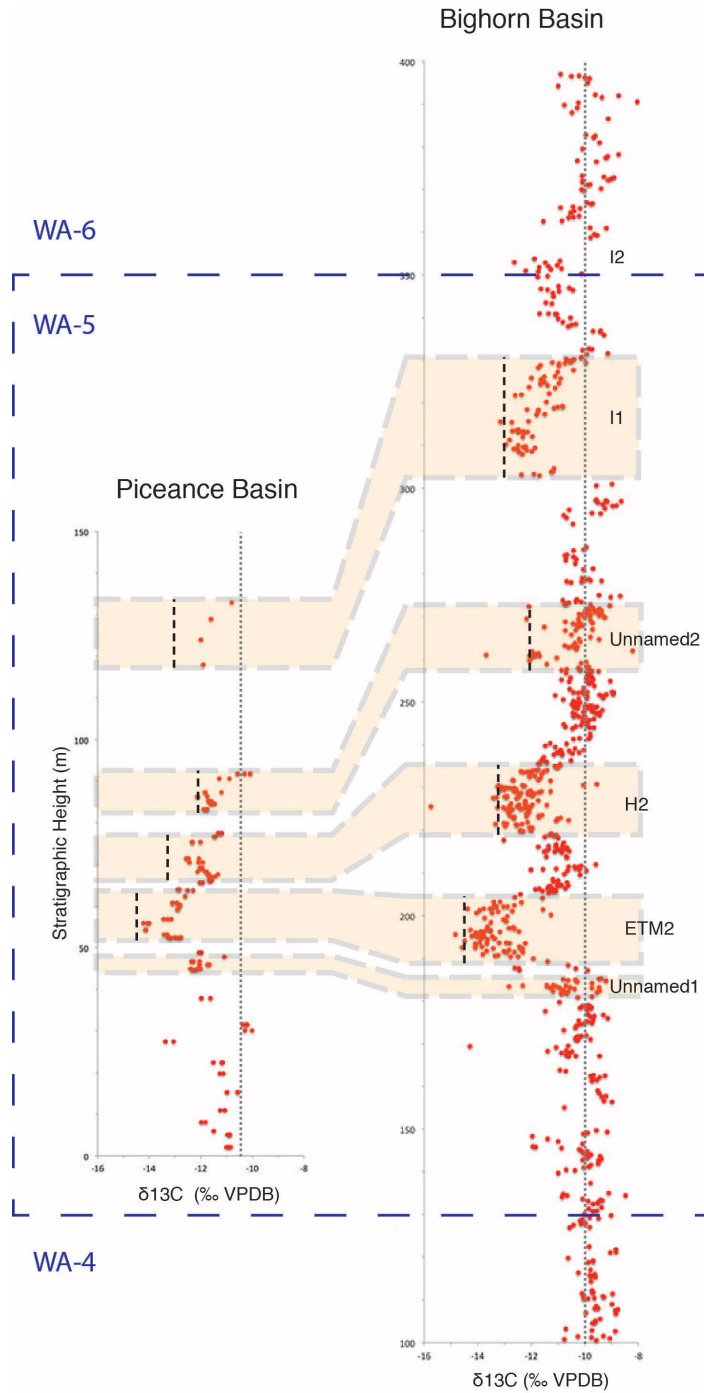
The two carbon isotope records are plotted, one from the Piceance Basin on the left and one from the Bighorn Basin (Abels et al., 2015) on the right. Wasatchian faunal zones are outlined in purple. Tan bars delineate interpreted chemostratigraphic correlations between the named hyperthermals in the Bighorn Basin and the newly discovered hyperthermals in the Piceance Basin. All carbon isotope data is plotted against PDB. Data for Piceance Basin is located in Table 1. Thin dashed lines indicate average background values, while thick dashed lines indicate maximum δ¹³C values of hyperthermals identified in the Bighorn Basin.

Figure 8) δ¹⁸O comparison for PB and BHB
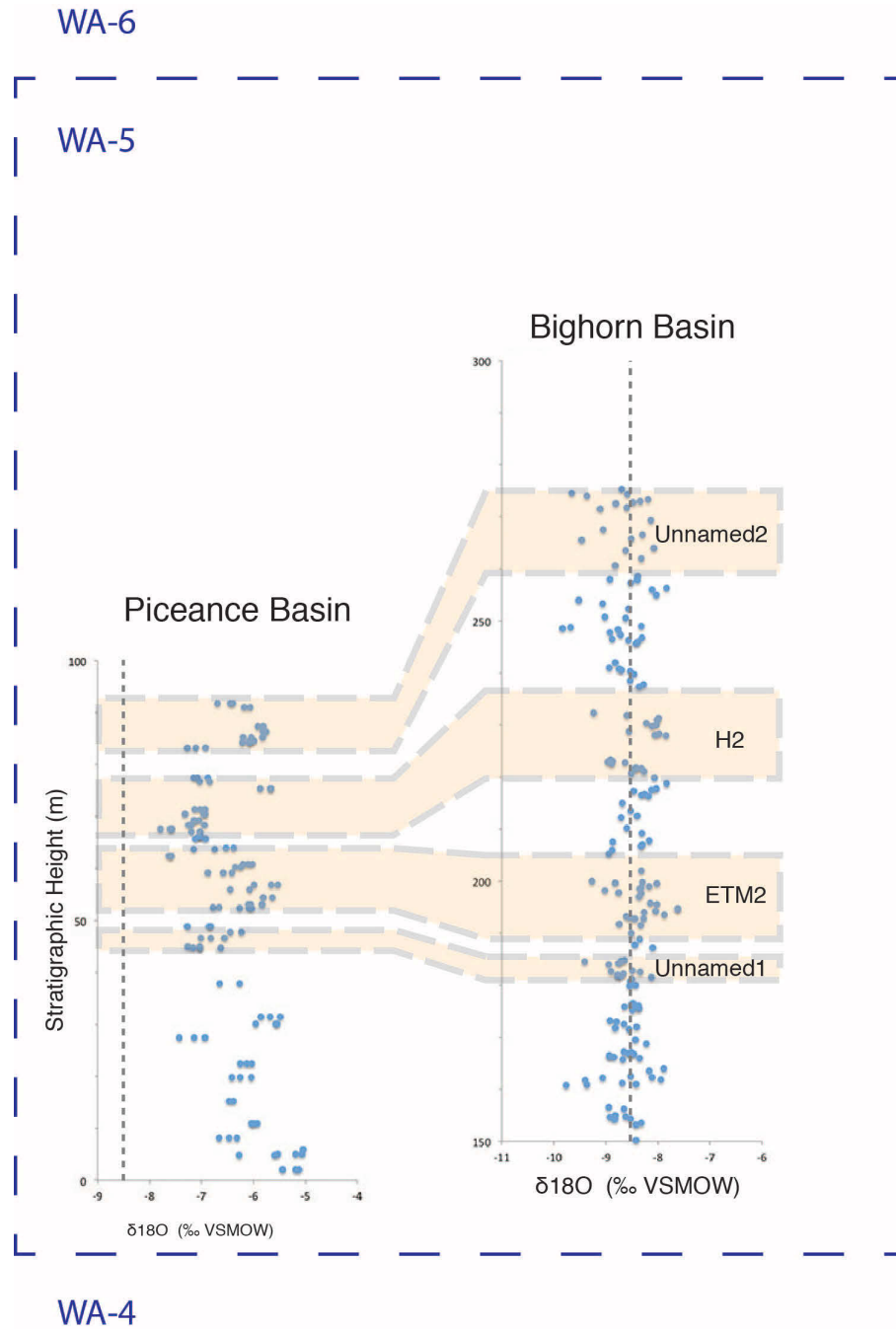
The two oxygen isotope records are plotted, one from the Piceance Basin on the left and one from the Bighorn Basin (Abels et al., 2015) on the right. Wasatchian faunal zones are outlined in purple. Tan bars delineate interpreted chemostratigraphic correlations between the named hyperthermals in the Bighorn Basin and the newly discovered hyperthermals in the Piceance Basin. All oxygen isotope data is plotted against SMOW. Data for Piceance Basin is located in Table 1. Thin dashed lines indicate average δ¹⁸O values for the Bighorn Basin.

Figure 9) CALMAG comparison for PB and BHB
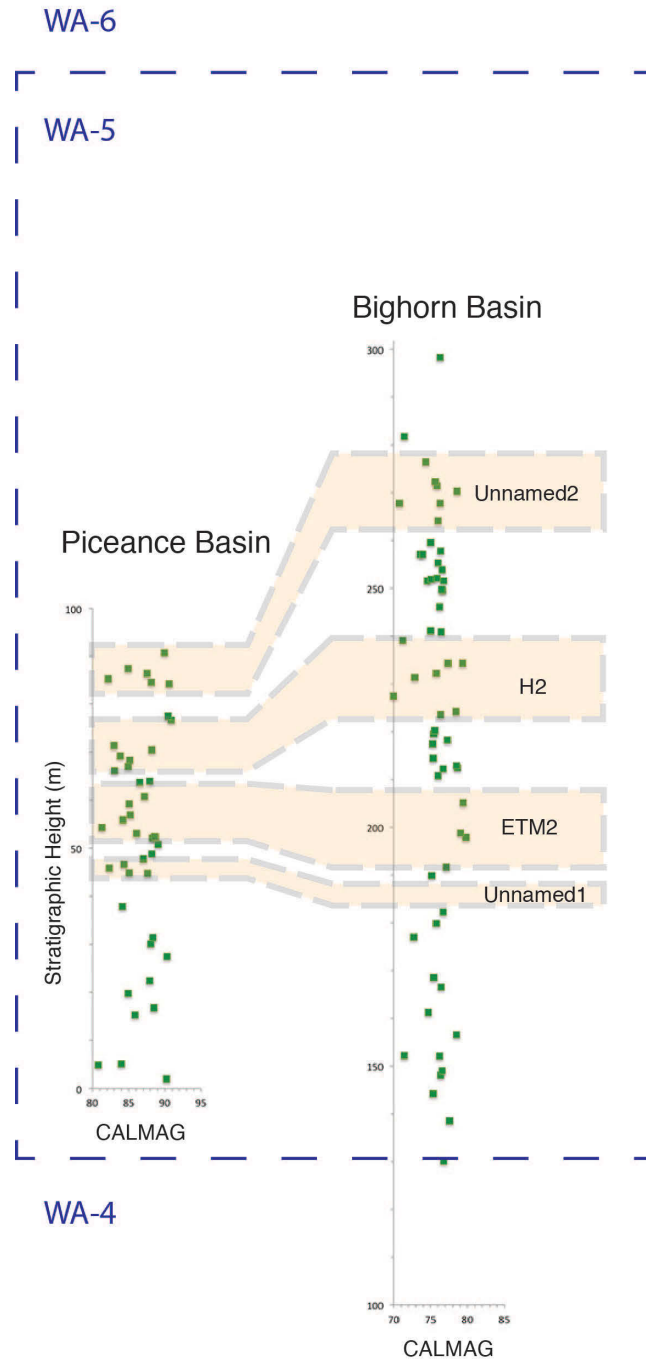
The two CALMAG curves are plotted, one from the Piceance Basin on the left and one from the Bighorn Basin (Abels et al., 2015) on the right. Wasatchian faunal zones are outlined in purple. Tan bars delineate interpreted chemostratigraphic correlations between the named hyperthermals in the Bighorn Basin and the newly discovered hyperthermals in the Piceance Basin. CALMAG regressions were taken from Nordt and Driesse (2009). Data for Piceance Basin are given in Table 2.

Figure 10) CALMAG and AL/Si Graphs
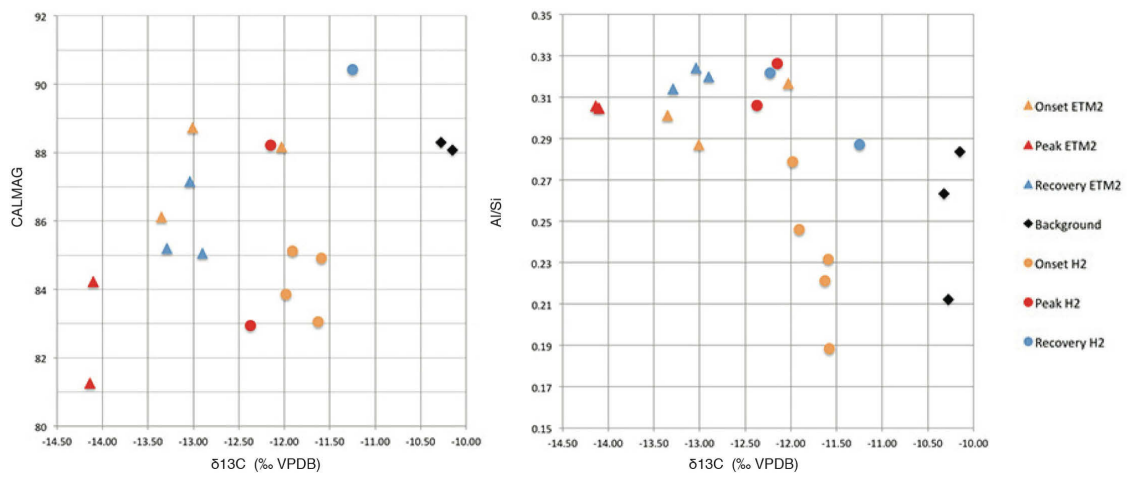
The CALMAG and Al/Si weathering indices for paleosols in the Piceance Basin are plotted against δ¹³C (‰ VPDB). Data from the onset, peak and return of both ETM2 and H2 are plotted along with the few background values present in the Piceance Section. The CALMAG ratio is developed by Nordt and Driesse (2010). Data are compiled in Table 2.

Figure 11) Soluble/Insoluble Ion Graphs
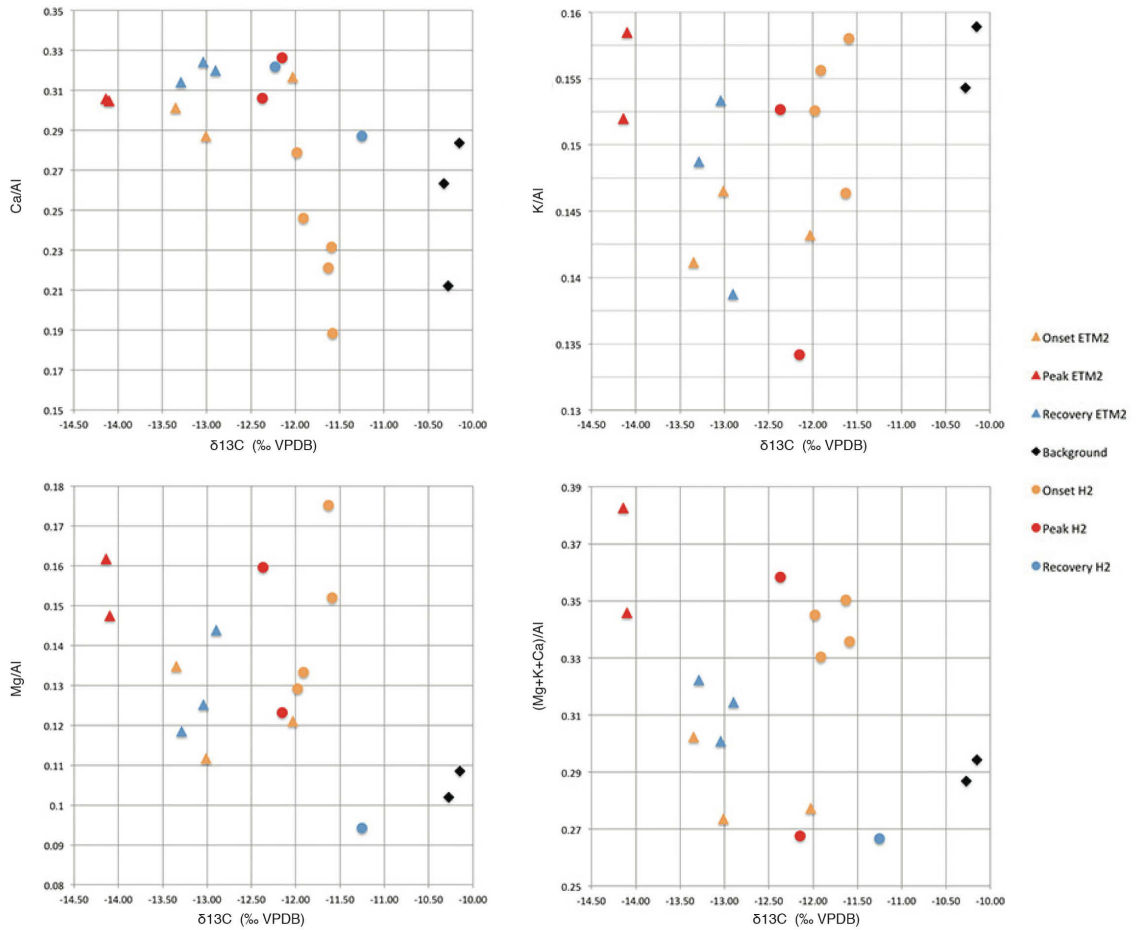
Figure 11

The base/insoluble weathering indices for paleosols in the Piceance Basin are plotted against δ^{13}C (‰ VPDB). Data from the onset, peak and return of both ETM2 and H2 are plotted along with the few background values present in the Piceance Section. (Mg+K+Ca)/Al was developed by Sheldon and Tabor (2009). Data are compiled in Table 3.

Figure 12) Fe and Mn Graphs
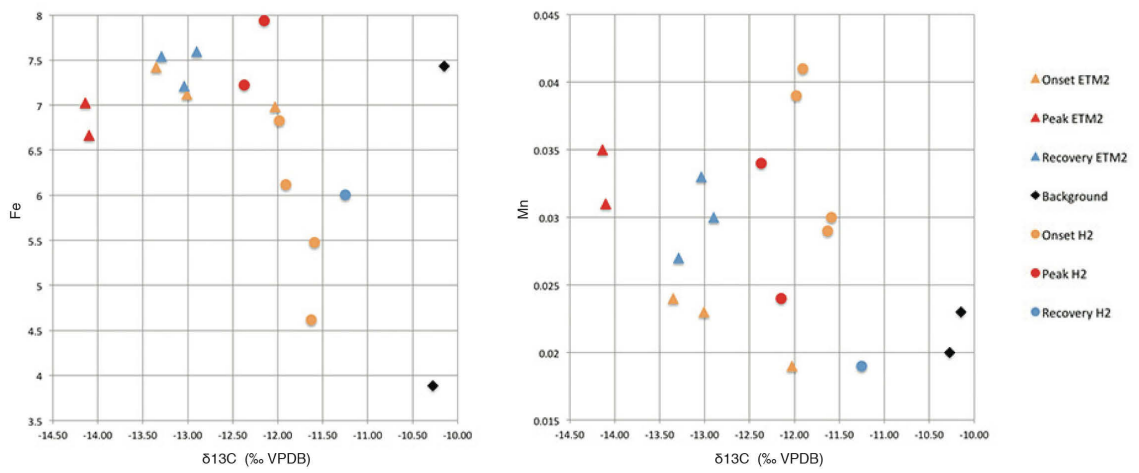
Figure 12

Fe and Mn weight percentages for paleosols in the Piceance Basin are plotted against $\delta^{13}C$ (‰ VPDB). Data from the onset, peak and return of both ETM2 and H2 are plotted along with the few background values present in the Piceance Section. These plots are good indicators of redox conditions. Data are compiled in Table 4.

5) Discussion

5.1) Carbon Isotopes: Stratigraphy and Sedimentation

5.1.1) Identifying Hyperthermal Events in the Piceance Basin

Previous work has demonstrated that hyperthermal events are characterized by a negative shift in $\delta^{13}C$ due to an increase in the flux of ^{12}C into the exogenic carbon reservoir (Bowen et al., 2006; Zachos et al., 2008; Abels et al., 2012). The source and mechanism is still undefined (DeConto et al., 2010; Westerhold et al., 2009; Moore and Kurtz, 2008; Dickens et al., 2007; Higgins and Schrag, 2006). Despite negative CIEs can still be utilized to identify hyperthermal events (Koch et al., 1992; McInerny and Wing, 2011). Plotting the $\delta^{13}C$ value with respect to stratigraphic position for the Piceance Basin, and then comparsing the $\delta^{13}C$ curve to a known and studied curve in the Bighorn Basin, allows for chemostratigraphic correlation of Piceance Basin strata to hyperthermal events identified in the Bighorn Basin (Figure 6, Figure 7) (Abels et al., 2015).

Background, or non-hyperthermal, $\delta^{13}C$ values for the Bighorn Basin range from -10‰ to -11‰. Hyperthermal Events ETM2, H2, I1, and I2 (Abels et al., 2015) on the Bighorn Basin curve have average minimum $\delta^{13}C$ values of -14.5 ‰, -13.4 ‰, -12.9 ‰, and -12.0 ‰, respectively. The $\delta^{13}C$ curve for the Piceance Basin indicates four negative CIEs with approximate minimum $\delta^{13}C$ values of -14.2 ‰, -12.5 ‰, -12.1 ‰, and -12.2 ‰ (Figure 7; Table 1).

Four hyperthermal events were identified in the Piceance Basin through chemostratigraphic correlation with the Bighorn Basin δ^{13}C curve (Abels et al., 2015). These events included ETM2, H2, an unnamed CIE and I1 (Figure 7). Minimum δ^{13}C values were compared between basins (Figure 6, Figure 7), and CIEs with the most similar values, which were also similarly situated with respect to surrounding CIEs, were interpreted as the same events. Thicknesses for the CIEs in the Piceance Basin are estimated based on the shapes of the curves in comparison with the Bighorn Basin section.

In addition to having four CIEs with similar minimum δ^{13}C values in both the Piceance Basin and the Bighorn Basin, the two sections are located in the same biostratigraphic zone. The biostratigraphic constraints in the form of WA 5 mammal fossils in both field areas provides a relative time constraint and indicates that the Piceance Basin study locality, similar to the Bighorn Basin, contains early Eocene strata (Abels et al., 2012; Burger, personal communication).

5.1.2) Sedimentation Rates in the Piceance Basin

Correlation with the Bighorn Basin section indicates that there are differences in sedimentation between basins; background δ^{13}C values and associated nodules are not recorded in the Piceance Basin section. The four hyperthermal events recorded in the Piceance Basin transect are included within ~85 m of stratigraphic section while the same stratigraphic sequence in the

Bighorn Basin is ~150 m thick (Figure 6; Figure 7). Consequently, it appears that sedimentation in the Piceance Basin is tied to hyperthermal events.

The Bighorn Basin appears to contain a complete sedimentary record, including isotopic data, from carbonate nodules (Figure 8). Consequently Abels et al. (2013) and Abels et al. (2015) were able to provide well-constrained long-term sedimentation rates for the Bighorn Basin. Utilizing procession cycles in the Eocene of ~20 ky (Abels et al., 2015, Stap et al., 2010) they estimated an average sedimentation rate of ~3.5 m/ky, which results in ~96 ky for the 34 m of strata corresponding to the ETM2 and H2 interval (Abels et al., 2015).

The Piceance Basin transect is characterized by thick stacked paleosols formed during CIEs that are separated by thin, centimeter to meter thick, sheet sandstones and lenticular sandstone deposits, all interspersed with thin paleosol units that record background values. The thickness of these non-hyperthermal units cannot account for all of the non-hyperthermal time separating hyperthermal events if a constant sedimentation rate is assumed. Consequently there is either missing section or the sedimentation rate was drastically reduced between hyperthermal events.

Unlike the Bighorn Basin where consistent sedimentation rates are assumed, the nature of strata in the Piceance Basin does not give confidence for long-term sedimentation rate calculations, as sedimentation appears to have been more pulsed in nature. The apparent variation in sedimentation rate and nature, between hyperthermal and non-hyperthermal times, is intriguing and

integral to our understanding of environmental change during ETM2 and H2 in the Piceance Basin. This interpretation will be discussed in more detail in section 5.4.

5.2) Oxygen Isotopes: Proxies for Aridity and Moisture Transport

Differences in the $\delta^{18}O$ values of carbonate nodules between the Piceance Basin and the Bighorn Basin may allow for interpretations of regional variance of temperature and aridity. The oxygen isotopic composition of authigenic soil carbonate is controlled by two factors: (1) a temperature dependent fractionation of oxygen isotopes during carbonate formation, and (2) the $\delta^{18}O$ of water present in the soils. The $\delta^{18}O$ of soil water is controlled by both aridity and the $\delta^{18}O$ of the precipitation. Soil water and meteoric water are similar in isotopic composition for a region, with soil water being approximately offset by 2 ‰ to 10 ‰ due to evaporative loss of ^{16}O. The $\delta^{18}O$ values for meteoric water are dependent on the source of the water and the rainout history of the region's precipitation. Lower $\delta^{18}O$ values occur with increasing progressive (Rayleigh) distillation of a particular air mass as it moves across a continent.

Higher temperatures result in less fractionation during carbonate precipitation, and consequently more negative $\delta^{18}O$ values in carbonate. However, higher temperatures would also result in more positive $\delta^{18}O$ values of meteoric water, due to evaporation, which would work to counteract the negative shift in $\delta^{18}O$ due to less fractionation during carbonate formation (Koch et al., 2003). As a result, changes in the $\delta^{18}O$ of authigenic carbonate are recording the

combined effects of a multitude of factors, therefore complicating their interpretation.

There are two major differences observed between the oxygen isotope curves from the Bighorn Basin and the Piceance Basin: (1) the $\delta^{18}O$ records indicate a 2.15 ‰ variance in average $\delta^{18}O$ values between the two basins, and (2) the Piceance Basin $\delta^{18}O$ curve is much more structured than the Bighorn Basin Curve (Figure 6; Figure 8). The Bighorn Basin (Abels, unpublished) records indicate $\delta^{18}O$ values with an average of -8.6 ‰, while the Piceance Basin records indicate an average $\delta^{18}O$ of -6.45 ‰ (Figure 8).

5.2.1) Effects of Rayleigh Distillation on Interbasin $\delta^{18}O$ Variance

To constrain the effects of Rayleigh distillation on differing $\delta^{18}O$ values between the Piceance Basin and the Bighorn Basin, Paleogene mammal $\delta^{18}O$ records from both basins were compared. As mammals maintain a constant body temperature there is no variance in the temperature-dependent fractionation of oxygen as it is incorporated into apatite in the mammals teeth. Consequently the $\delta^{18}O$ values from mammals reflect the $\delta^{18}O$ values of the meteoric water. Secord et al. (2008) measured $\delta^{18}O$ values from a variety of taxa in the Bighorn Basin. Their results indicate an average $\delta^{18}O$ of 20.79 ‰. Hillary Christianson (unpublished) calculated an average $\delta^{18}O$ of 22.10 ‰ for mammals in the Piceance Basin.

The -1.31 ‰ shift in the mammalian $\delta^{18}O$ between the two basins reflects the ^{18}O rainout as the moisture progresses northward from the Piceance to the

Bighorn Basin. As a – 2.15 ‰ decrease was noted in nodules, only 1.31 ‰ can be accounted for due to rainout of ^{18}O. The remaining 0.84 ‰ must be the result of either temperature-dependent fractionations or the effect of evaporation on meteoric water.

Eocene climate models indicate that both the Piceance Basin and the Bighorn Basin receive moisture from the same source. Recent models indicated that moisture originated in the Mississippi Embayment and traveled north and westward, first interacting with the Piceance Basin and then the Bighorn Basin (Sewall and Sloan, 2006).

This model has recently been revised (Fricke and Sewall, unpublished), shifting the moisture source to the Pacific Ocean. The north–south striking Sevier uplift that separated the Pacific Ocean from the Laramide basins (Davis et al., 2009), including both the Piceance Basin and the Bighorn Basin, forced the Pacific moisture south before it could make its way across the continent. Consequently, when the moisture circumvented the Sevier uplift, it began to move south to north, similar to the Sewall and Sloan (2006) model. The outcome of northward moving moisture results in a northward progressing Rayleigh Distillation that would produce more negative $\delta^{18}O$ values in the Bighorn Basin than the Piceance Basin.

The 0.84 ‰ difference that is not accounted for by Rayleigh distillation must be the result of temperature or aridity variation between basins. Increases in temperature reduce the fractionation during nodule formation, resulting in lower

$\delta^{18}O$ values, while increases in aridity result in higher $\delta^{18}O$ values. Consequently the 0.84 ‰ decrease from the Piceance Basin to the Bighorn Basin is either the result of the Bighorn Basin having been ~3° warmer than the Piceance Basin (Kim and O'Neil, 1997), or the Piceance Basin having been drier than the Bighorn Basin.

5.2.2) Changes in Aridity during ETM2 in the Piceance Basin

The $\delta^{18}O$ record from the Bighorn Basin (Abels, unpublished) displays fairly uniform $\delta^{18}O$ values, whereas the record for the Piceance Basin indicates more variability in $\delta^{18}O$. The $\delta^{18}O$ values in the Bighorn Basin range from -8.0 ‰ to -9.0 ‰, and in the Piceance Basin range from -5.0 ‰ to -7.8 ‰ (Figure 8).

In both basins temperature increased during hyperthermal events, which should have resulted in lower $\delta^{18}O$ values. However, this expected trend is not present in either the Bighorn Basin or the Piceance Basin data. This phenomenon can be explained if during warming there was an associated aridification effect that resulted in increased evaporation. Increased evaporation counteracts the effect of decreased fractionation due to temperature, and consequently the expected decrease in $\delta^{18}O$ during the hyperthermals may not have been realized (Koch et al., 2003).

ETM2 in the Piceance is different as it indicates a clear positive shift in $\delta^{18}O$ during the event. We interpreted this positive shift to be the result of increased aridity in the Piceance Basin during ETM2. As this pattern is not

observed in the Bighorn Basin $\delta^{18}O$ sequence, it suggests that changes in aridity were much more pronounced in the Piceance Basin.

5.3) Weathering Indices

Standard weathering indices rely on the property that the base-forming oxides CaO, MgO, Na_2O and K_2O are depleted with respect to Al_2O_3 with increased precipitation. The base oxides are soluble and therefore ionize, and are thus removed from the system when more water is present. CALMAG $[Al_2O_3/(Al_2O_3 + CaO + MgO) \times 100]$ is a variation on standard weathering indices that has improved accuracy for vertisols. Na_2O was removed to reduce the affect of differential inheritance and weathering of sodium bearing minerals (Nordt and Driese, 2010).

For all these proxies, it is assumed that the time a soil is sitting on the surface is constant and therefore the degree of weathering, or grain size, is solely due to weathering intensity, or transport capacity, and not weathering time, or the presence of weathering.

CALMAG values are typically associated with MAP estimates (Nordt and Driese, 2010), but the relationship and numerous confounding factors are complex and not fully understood. Instead of providing MAP estimates, CALMAG values are only used as a proxy for relative weathering and precipitation for the Piceance Basin. High CALMAG values correspond to increased weathering, increased soil moisture, and removal of base cations.

Al/Si is a commonly utilized proxy for weathering intensity in paleosols. It is considered to also capture the clay content of a soil relative to a Si bearing parent material. Typically, an increase in weathering intensity will result in relative increase in the Al content of the paleosol (Sheldon and Tabor, 2009) and therefore an increase in the Al/Si ratio of the paleosol.

Base/insoluble ion ratios are commonly utilized as hydrolysis proxies for paleosols. Ca/Al, K/Al, Mg/Al and (Ca+K+Mg+Na)/Al are all common ratios used to better understand the degree of weathering in a paleosol. Soluble or base cations include Ca, Na, K, and Mg. Under more intense weathering the base cations will be mobilized and removed from the system before the insoluble ions like Al (Sheldon and Tabor, 2009). Consequently, changes in the ratio of soluble/insoluble ions can be used to infer weathering intensity. Increased weathering corresponds to lower ratios and vice versa for decreased weathering.

Mn and Fe were analyzed to investigate redox conditions in the soils. Both manganese and iron are redox-sensitive elements, as they are sensitive to the oxygen availability of their surrounding environments. In oxidized environments both Fe and Mn are insoluble, and in reducing conditions they are highly mobile. The overall Fe or Mn content in soils can therefore be used as a proxy for the presence of groundwater. Wet environments tend to be associated with reducing conditions and therefore lower quantities of Fe and Mn.

5.3.1) CALMAG

For all CIEs recorded in the Piceance Basin section, CALMAG weathering indices decrease from the onset through to the peak of the CIE. The initial decrease is then followed by an increase in CALMAG values through the return of the associated CIE (Figure 9). The common trend realized in all four identified hyperthermal events (Figure 6; Figure 9; Figure 10) in the Piceance Basin indicates that there is a decrease in weathering from the onset through peak δ^{13}C excursion values. Weathering intensity then increases back towards initial values through the return.

5.3.2) Al/Si

For both ETM2 and H2 sequences, there appears to be an observed increase in the Al/Si ratio from background values to those of the hyperthermals, but the relationship is not clear (Figure 10; Table 2). The increase might reflect intensification in weathering during the peaks of the hyperthermals which would contradict the CALMAG, (Ca+K+Mg+Na)/Al, Ca/Al, K/Al, and Mg/Al proxies (Figure 10, Figure 11).

There is, however, an alternate interpretation of the Al/Si ratio, namely that it reflects grain size and fluvial transport energy of the sediment, rather than weathering. Sediment closer to the sediment source will generally have both a larger grain size and higher quartz, feldspar and Si content, while sediment more distal to the source will generally be smaller, more clay rich, and consequently will have more Al and less Si (Marce et al., 2006). Thus, the noted increase in

Al/Si through the onset and peak hyperthermal periods may reflect an increase in clay content.

5.3.3) Other Soluble/Insoluble Weathering Indices

There an increase in Ca/Al, Mg/Al and Σbase/Al ratios and a decrease in K/Al from background to peak hyperthermal values (Figure 11; Table 3). The increase in Mg/Al, Ca/Al and Σbase/Al of hyperthermal event deposits reflects a decrease in weathering intensity. The variability noted in K/Al may have arisen due to a decrease in weathering of K-bearing parent material during hyperthermal events, or it may have resulted from weathering of a low K parent, and consequently there was little input of K into the system during hyperthermal events. The Σbase/Al index provides better coverage for weathering of non-silicate parent materials (Sheldon and Tabor, 2009) and takes into account the variation that may arise in the individual soluble/insoluble ion ratios, as with K/Al.

5.3.4) Redox Proxies

There appears to be an increase in both Fe and Mn content during hyperthermal events (Figure 12; Table 4). The increase noted in Mn is more pronounced and better constrained than for Fe. This increase in both Fe and Mn indicates a more oxidized environment during hyperthermal events, potentially corresponding to an overall decrease in soil moisture and a transition to more seasonal precipitation in the Piceance Basin.

5.3.5) Combined Interpretations

All weathering proxies based on soluble/insoluble ions, with the exception of K/Al, suggest a decrease in weathering intensity from onset to peak δ^{13}C values during hyperthermal events. From the peak δ^{13}C values through the end of the CIE, weathering intensity apparently increased again. The inferred decrease in weathering during all captured hyperthermal events in the Piceance Basin, is consistent with aridification during the Eocene hyperthermals, as suggested from δ^{18}O records (Section 6.2). Redox sensitive elements support the above interpretations, suggesting a decrease in soil moisture that may correspond to an overall decrease in precipitation during hyperthermal events, or a transition to more seasonal precipitation patterns. The subsequent increase in weathering intensity suggested for the hyperthermal return is the adjustment of local environments to background conditions (Figure 9, 10, 11, and 12).

The Piceance Basin differs from the Bighorn Basin in that the apparent decrease in weathering (Figures 6, 10, and 11) noted in the Piceance Basin is not evident in the Bighorn Basin data. In fact, CALMAG curves for the Bighorn Basin indicate that weathering intensity in the Bighorn Basin actually increases slightly during ETM2, H2, and a third unnamed hyperthermal (Figure 6).

5.4) Linking Climate to Sedimentation in the Piceance Basin: A Model

Sedimentation appears to be tied to hyperthermal events in the Piceance Basin. Furthermore, environmental conditions changed during hyperthermal

events. The goal is to explain the observations through development of a basin sedimentation model.

Sediment flux in modern basins is primarily controlled by climate, topography, and lithology of the source material (Bierman and Montgomery, 2014). Lithology of the source material influences sediment flux as the competency of material determines sediment supply, which in turn contributes to sediment flux. Topography influences the sediment flux in that uplift, and therefore increasing stream gradients, result in an increase in accommodation space, as well as amplified stream power. The combined effects contribute to the sediment flux through increased erosional power, transport capacity, and accommodation space. The influence of climate includes the amount of precipitation, and therefore weathering rates of bedrock, as well as transport capacity of weathered sediment (Bierman and Montgomery, 2014).

Various studies, (Campbell, 1977; Leeder et al., 1998; Brady et al., 2012; Mueller and Pitlick, 2013) have indicated that lithology is the primary control on sediment supply and flux in terrestrial basins. Basin relief and climatic factors are secondary. Carroll et al. (2006) indicate that deposition in sedimentary basins depends on a combination of tectonic controls on accommodation space, as well as climatic controls on hydrology. Assuming that source material lithology for the Piceance Basin did not change from hyperthermal to non-hyperthermal times (time scale of 10 ky), and the timescale for the ETM2 – H2 interval was ~ 96 ky

(Abels et al., 2015), neither lithology nor topographic change likely impacted the sedimentary flux into the Piceance Basin (Dickenson et al., 1988).

Thus, climate is the remaining factor that acted as a major control on sediment flux into the Piceance Basin. Climate's influence on sediment flux manifests in two ways (Bierman and Montgomery, 2014): (1) its impact on sediment production due to chemical and physical weathering of parent material, and (2) its impacts on sediment transport as a function of fluvial discharge. Chemical and physical weathering impact sediment flux because increased weathering results in an increased sediment supply. A greater sediment supply leads to more material available for transport and therefore increased sediment flux. Increased discharge bolsters the fluvial transport capacity of streams and rivers, which therefore increases the sediment flux as well. Variations between the two components described above result in differing sediment fluxes during hyperthermal and non-hyperthermal events and therefore differing sedimentation rates.

5.4.1) Hyperthermal Sedimentation

Based on geochemical proxies described previously, it appears that hyperthermal events were associated with (1) an increase in temperature, (2) a decrease in weathering, and (3) aridification (Figure 6). In addition, there was a qualitative increase in grain size during hyperthermal events, and the occurrence of carbonate nodules implies a more seasonal precipitation pattern. These

observations are predicted to have had the following impact on basin sedimentation.

Aridification, as well as proxies suggesting decreased weathering, which could imply an overall decrease in rainfall and soil moisture, are instead interpreted as the result of a more seasonal climate. During the hyperthermal events, precipitation was likely condensed into less frequent, higher intensity, wet seasons that were separated by longer and more powerful dry seasons during which evaporation increased (Koch et al., 1998). The result of less frequent, but higher volume, precipitation events, was less frequent but higher intensity fluvial discharge events. As discharge is directly related to transport capacity, higher discharge led to increased transport capacity, resulting in greater sedimentation rate, as well as deposition of larger clast sizes, both of which are observed for the Piceance section (Bierman and Montgomery, 2014) (Figure 13).

A consequence of the more intense but sporadic precipitation events during hyperthermals is that these events would have stripped much of the weathered regolith from the sediment source during the hyperthermal event. Consequently, during the transition to background $\delta^{13}C$ values, there may have been less weathered material available for transport and deposition in the basin. Additionally, during the transition from background $\delta^{13}C$ values to a hyperthermal event, the environmental changes, namely increased discharge, would have removed much of the fine-grained material deposited between hyperthermals as the landscape re-equilibrated to climactic changes. Thus, less background

sediment was preserved, and by the time the landscape re-equilibrated to the new climate regime, and both carbonate nodules and paleosols start forming, the $\delta^{13}C$ values shifted.

Figure 13) Schematic Detailing Sedimentation During Hyperthermals
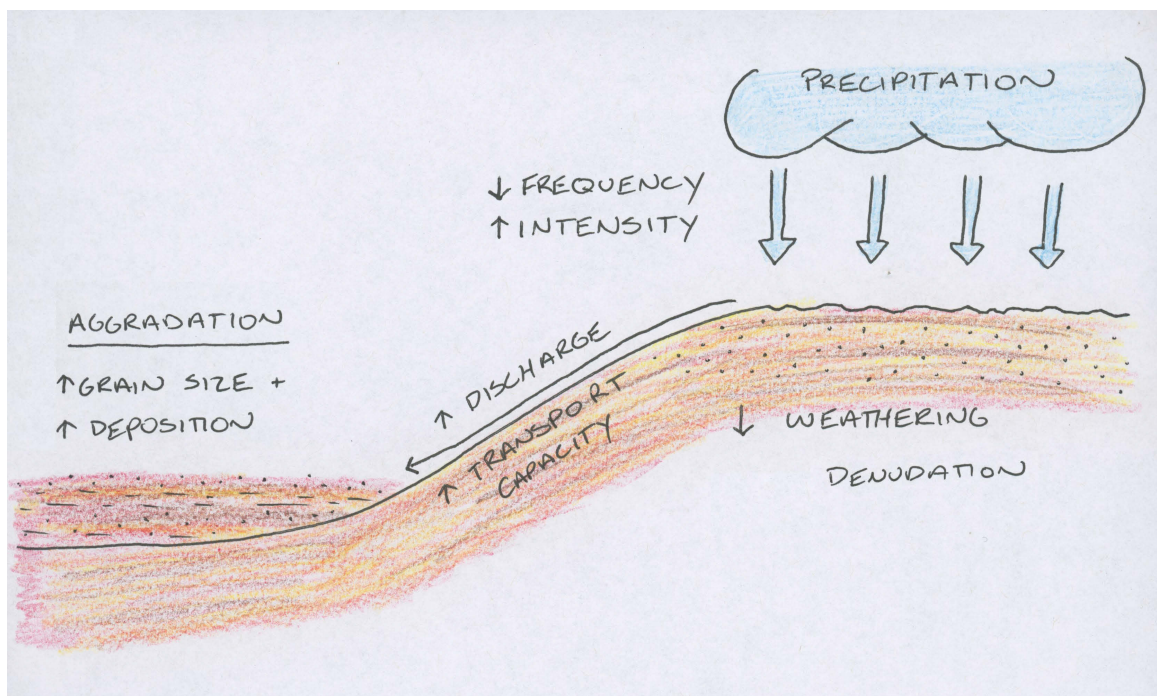
This schematic details the relationship between precipitation, weathering, discharge, transport and deposition during hyperthermal times for the proposed sedimentation model.

5.4.2) Non-hyperthermal Sedimentation

Between hyperthermal events, (1) temperature decreased, (2) weathering increased, (3) soil moisture increased and (4) grain size decreased in relation to hyperthermal conditions. The increase in soil moisture or "wetting" trends either suggests more precipitation in total, or more constant yet less intense precipitation. As carbonate nodules are not present in strata recording times between events, and there is no evidence for significant increases in mean annual precipitation, such times are interpreted as having had more frequent and lower intensity precipitation events. These intervals correlate to more frequent but lower discharge events which resulted in decreased overall fluvial transport capacity (Bierman and Montgomery, 2014). Decreased transport capacity corresponds to diminished accumulation rates, as well as a reduced capacity to transport large clasts. Both of these are supported by stratigraphic data (Figure 14).

As much of the weathered regolith would have been stripped during the increased discharge events during hyperthermals, there was little to no weathered material available for transport, which would have contributed to the interpreted diminished sedimentation rates between hyperthermals. As weathering appears to have increased between hyperthermal events, and both discharge and transport capacity may have decreased, weathered regolith would have accumulated until it was mobilized under increased discharge during hyperthermal events.

Figure 14) Schematic Detailing Sedimentation Between Hyperthermals
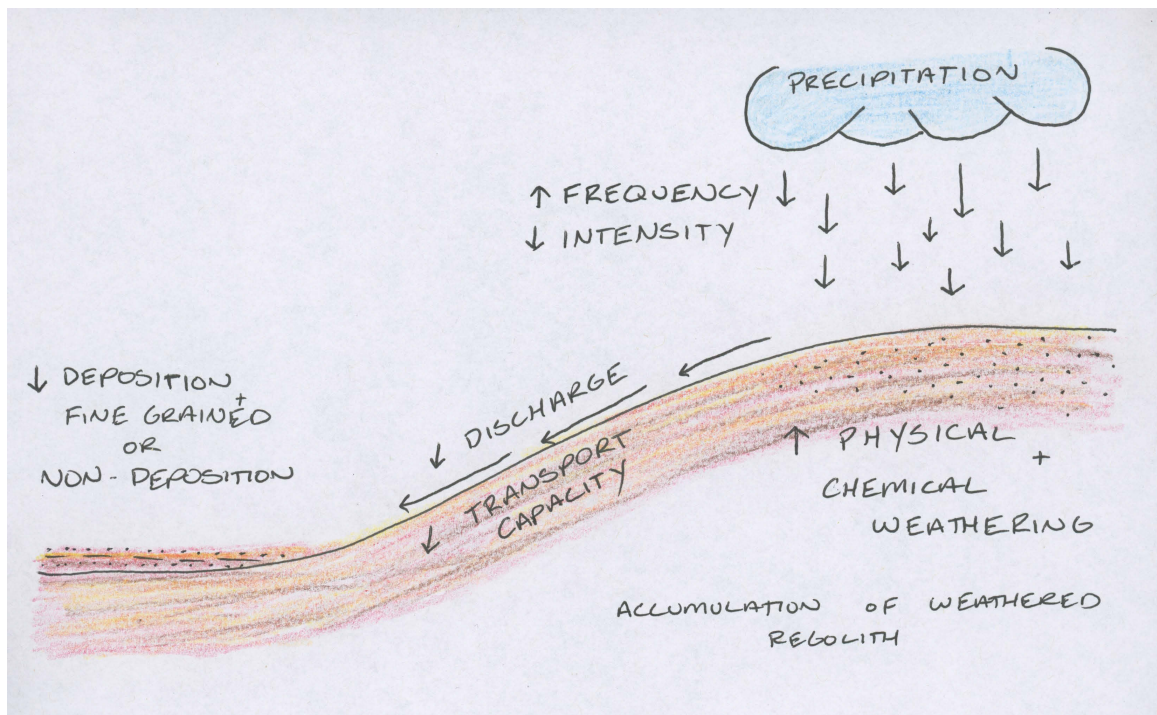
This schematic details the relationship between precipitation, weathering, discharge, transport and deposition during non-hyperthermal times for the proposed sedimentation model.

6) Conclusion

Comparison of environmental impacts between the Bighorn Basin and the Piceance Basin reveals that there is much regional variation in terms of sedimentation, weathering, and precipitation patterns during the ETM2 hyperthermal event. In the Bighorn Basin, the ETM2 was characterized by a temperature increase, a decrease in $\delta^{13}C$, little to no increase in soil moisture or weathering, no indication of seasonality, no associated floral or faunal turnover, and no apparent large changes in sedimentation.

The ETM2 record in the Piceance Basin is similar on some levels, as there is evidence for an accompanying temperature increase, a decrease in $\delta^{13}C$, and no associated floral or faunal turnover. However, the ETM2 record in the Piceance Basin differs drastically from the Bighorn Basin, as it suggests a decrease in weathering during the hyperthermal event, a decrease in soil moisture, strong evidence for seasonal precipitation, and a drastic change in sedimentation flux.

Comparison of $\delta^{13}C$ curves for the Bighorn Basin and the Piceance Basin reveals large differences in the preservation of hyperthermal events between the two basins. The Bighorn Basin record indicates more continuous sedimentation between and during hyperthermal events. The Piceance Basin on the other hand shows drastically reduced sediment preservation between hyperthermal events, and increased sediment preservation during hyperthermal events.

My sedimentation model for the Piceance Basin proposes that more seasonal precipitation, and therefore increased fluvial discharge, resulted in increased sediment transport and sedimentation rates during hyperthermal events. This increase in sediment transport would have stripped the weathered regolith from the highlands, therefore limiting available sediment for transport between hyperthermal events. A secondary side effect of increased discharge associated with hyperthermal events, is that at the onset of a hyperthermal event the increased discharge would erode some of the non-hyperthermal sediment, resulting in less preservation of non-hyperthermal sediment.

Between hyperthermal events, precipitation patterns were less seasonal, may have resulted in more frequent and less intense precipitation events. The resulting decrease in discharge results in lower sedimentation rates. The outcome of the aforementioned factors is expressed in a sedimentary package primarily preserving hyperthermals in the Piceance Basin.

Comparing ETM2 environmental impacts for both the Bighorn Basin and the Piceance Basin with published PETM environmental changes from the Bighorn basin, once again reveals that hyperthermal events are not all characterized by the same environmental changes in precipitation regimes, weathering intensity, sedimentation rates, and floral and faunal turnover. The PETM in the Bighorn Basin is similar to the ETM2 event in that it is characterized by an increase in temperature and a decrease in $\delta^{13}C$. However, the magnitude of the variance in the temperature and the $\delta^{13}C$ varies greatly between events.

The PETM resulted in ~ 4–7 °C temperature increase and a -4.7‰ ± 1.5‰ decrease in $\delta^{13}C$, while ETM2 resulted in ~ -3-5 °C temperature increase and approximately -1.5 ‰ to -2.0 ‰ decrease in $\delta^{13}C$.

The PETM was also characterized by a well-defined floral and faunal turnover, an impact not identified during ETM2. Similar to the ETM2 record in the Piceance Basin, but different from that in the Bighorn Basin, the PETM in the Bighorn Basin also resulted in decreased weathering and soil moisture, increased seasonality, and increased sediment production during the hyperthermal event.

As the environmental impacts of the ETM2 are becoming better defined, it is clear that there was variation in environmental changes between hyperthermal events. Careful consideration must be applied when extrapolating environmental impacts from one locality through time or space in order to characterize the nature of environmental change during hyperthermal events.

7) Future Work

Much more work is needed in the Piceance Basin in order to better understand the nature of environmental change during the ETM2. A more detailed and methodical sedimentary and grain size analysis would allow for better interpretation of sedimentary change. Higher resolution carbonate nodule sampling both along strike, and up section, in the basin would allow for compilation of a more robust $\delta^{13}C$ and $\delta^{18}O$ record that would potentially capture two more hyperthermal events higher in the section.

References Cited:

Abels, H.A., Lauretano, V., Yperen, A.v., et al., 2015, Carbon isotope excursions in paleosol carbonate marking five early Eocene hyperthermals in the Bighorn Basin, Wyoming: Clim.Past Discuss., v. 11, no. 3, p. 1857-1885.

Abels, H.A., Clyde, W.C., Gingerich, P.D., Hilgen, F.J., Fricke, H.C., Bowen, G.J., and Lourens, L.J., 2012, Terrestrial carbon isotope excursions and biotic change during Palaeogene hyperthermals: Nature Geosci, v. 5, no. 5, p. 326-329.

Abels, H.A., Kraus, M.J., and Gingerich, P.D., 2013, Precession-scale cyclicity in the fluvial lower Eocene Willwood Formation of the Bighorn Basin, Wyoming (USA): Sedimentology, v. 60, no. 6, p. 1467-1483.

Adams, J.S., Kraus, M.J., and Wing, S.L., 2011, Evaluating the use of weathering indices for determining mean annual precipitation in the ancient stratigraphic record: Palaeogeography, Palaeoclimatology, Palaeoecology, v. 309, no. 3, p. 358-366.

Aziz, H.A., Hilgen, F.J., Luijk, G.M.v., Sluijs, A., Kraus, M.J., Pares, J.M., and Gingerich, P.D., 2008, Astronomical climate control on paleosol stacking patterns in the upper Paleocene "lower Eocene Willwood Formation, Bighorn Basin, Wyoming: Geology, v. 36, no. 7, p. 531-534.

Bierman, P.R., and Montgomery, D.R., 2014, Key Concepts in Geomorphology, Macmillan Higher Education.

Bowen, G.J., Bralower, T.J., Delaney, M.L., et al., 2006, Eocene hyperthermal event offers insight into greenhouse warming: Eos, Transactions American Geophysical Union, v. 87, no. 17, p. 165-169.

Breecker, D., Sharp, Z., and McFadden, L.D., 2009, Seasonal bias in the formation and stable isotopic composition of pedogenic carbonate in modern soils from central New Mexico, USA: Geological Society of America Bulletin, v. 121, no. 3-4, p. 630-640.

Campbell, I., 1977, Stream discharge, suspended sediment and erosion rates in the Red Deer River basin, Alberta, Canada: Int.Assoc.Hydrol.Sci, v. 122, p. 244-259.

Carroll, A.R., Chetel, L.M., and Smith, M.E., 2006, Feast to famine: Sediment supply control on Laramide basin fill: Geology, v. 34, no. 3, p. 197-200.

Cerling, T.E., 1984, The stable isotopic composition of modern soil carbonate and its relationship to climate: Earth and Planetary Science Letters, v. 71, no. 2, p. 229-240.

Chew, A.E., 2009, Paleoecology of the early Eocene Willwood mammal fauna from the central Bighorn Basin, Wyoming: Paleobiology, v. 35, no. 01, p. 13-31.

Chun, C.O., Delaney, M.L., and Zachos, J.C., 2010, Paleoredox changes across the Paleocene-Eocene thermal maximum, Walvis Ridge (ODP Sites 1262, 1263, and 1266): Evidence from Mn and U enrichment factors: Paleoceanography, v. 25, no. 4.

Clyde, W.C., Hamzi, W., Finarelli, J.A., Wing, S.L., Schankler, D., and Chew, A., 2007, Basin-wide magnetostratigraphic framework for the Bighorn Basin, Wyoming: Geological Society of America Bulletin, v. 119, no. 7-8, p. 848-859.

Cowan, I., 1982, Regulation of water use in relation to carbon gain in higher plants. *In* Physiological Plant Ecology II, Springer, p.589-613.

Cramer, B.S., Wright, J.D., Kent, D.V., and Aubry, M., 2003, Orbital climate forcing of $\delta^{13}C$ excursions in the late Paleocene - early Eocene (chrons C24n - C25n): Paleoceanography, v. 18, no. 4.

Davis, S.J., Mulch, A., Carroll, A.R., Horton, T.W., and Chamberlain, C.P., 2009, Paleogene landscape evolution of the central North American Cordillera: Developing topography and hydrology in the Laramide foreland: Geological Society of America Bulletin, v. 121, no. 1-2, p. 100-116.

DeConto, R., Galeotti, S., Pagani, M., Tracy, D., Pollard, D., and Beerling, D., 2010, Hyperthermals and orbitally paced permafrost soil organic carbon dynamics, *in* AGU Fall Meeting Abstracts, p. 08.

Dickens, G.R., Castillo, M.M., and Walker, J.C., 1997, A blast of gas in the latest Paleocene: simulating first-order effects of massive dissociation of oceanic methane hydrate: Geology, v. 25, no. 3, p. 259-262.

Dickinson, W.R., Klute, M.A., Hayes, M.J., Janecke, S.U., Lundin, E.R., McKittrick, M.A., and Olivares, M.D., 1988, Paleogeographic and paleotectonic setting of Laramide sedimentary basins in the central Rocky Mountain region: Geological Society of America Bulletin, v. 100, no. 7, p. 1023-1039.

Donnell, J.R., 1969: Paleocene and lower Eocene units in the southern part of the Piceance Creek Basin, Colorado.

Egger, H., Homayoun, M., Huber, H., Rögl, F., and Schmitz, B., 2005, Early Eocene climatic, volcanic, and biotic events in the northwestern Tethyan Untersberg section, Austria: Palaeogeography, Palaeoclimatology, Palaeoecology, v. 217, no. 3, p. 243-264.

Foreman, B.Z., Heller, P.L., and Clementz, M.T., 2012, Fluvial response to abrupt global warming at the Palaeocene/Eocene boundary: Nature, v. 491, no. 7422, p. 92-95.

Hartley, A.J., Weissmann, G.S., Nichols, G.J., and Warwick, G.L., 2010, Large distributive fluvial systems: characteristics, distribution, and controls on development: Journal of Sedimentary Research, v. 80, no. 2, p. 167-183.

Higgins, J.A., and Schrag, D.P., 2006, Beyond methane: towards a theory for the Paleocene–Eocene thermal maximum: Earth and Planetary Science Letters, v. 245, no. 3, p. 523-537.

Hooker, J.J., 1998, Mammalian faunal change across the Paleocene-Eocene transition in Europe: Late Paleocene-Early Eocene climatic and biotic events in the marine and terrestrial records, p. 428-450.

Johnson, R.C., 2012, The systematic geologic mapping program and a quadrangle-by-quadrangle analysis of time-stratigraphic relations within oil shale-bearing rocks of the Piceance Basin, western Colorado, US Department of the Interior, US Geological Survey.

Kennett, J., and Stott, L., 1991, Abrupt deep sea warming, paleoceanographic changes and benthic extinctions at the end of the Paleocene.

Koch, P.L., Zachos, J.C., and Gingerich, P.D., 1992, Correlation between isotope records in marine and continental carbon reservoirs near the Paleocene Eocene boundary.

Koch, P.L., 1998, Isotopic reconstruction of past continental environments: Annual Review of Earth and Planetary Sciences, v. 26, no. 1, p. 573-613.

Koch, P.L., Clyde, W.C., Hepple, R.P., Fogel, M.L., Wing, S.L., and Zachos, J.C., 2003, Carbon and oxygen isotope records from paleosols spanning the Paleocene-Eocene boundary, Bighorn Basin, Wyoming: Special Papers-Geological Society of America, p. 49-64.

Kraus, M.J., 1997, Lower Eocene alluvial paleosols: pedogenic development, stratigraphic relationships, and paleosol/landscape associations: Palaeogeography, Palaeoclimatology, Palaeoecology, v. 129, no. 3, p. 387-406.

Kraus, M.J., McInerney, F.A., Wing, S.L., Secord, R., Baczynski, A.A., and Bloch, J.I., 2013, Paleohydrologic response to continental warming during the Paleocene–Eocene Thermal Maximum, Bighorn Basin, Wyoming: Palaeogeography, Palaeoclimatology, Palaeoecology, v. 370, p. 196-208.

Kraus, M.J., and Riggins, S., 2007, Transient drying during the Paleocene–Eocene Thermal Maximum (PETM): analysis of paleosols in the Bighorn Basin, Wyoming: Palaeogeography, Palaeoclimatology, Palaeoecology, v. 245, no. 3, p. 444-461.

Krishnan, S., Pagani, M., Huber, M., and Sluijs, A., 2014, High latitude hydrological changes during the Eocene Thermal Maximum 2: Earth and Planetary Science Letters, v. 404, p. 167-177.

Leeder, M.R., Harris, T., and Kirkby, M.J., 1998, Sediment supply and climate change: implications for basin stratigraphy: Basin Research, v. 10, no. 1, p. 7-18.

Lourens, L.J., Sluijs, A., Kroon, D., et al., 2005, Astronomical pacing of late Palaeocene to early Eocene global warming events: Nature, v. 435, no. 7045, p. 1083-1087.

Mack, G.H., James, W.C., and Monger, H.C., 1993, Classification of paleosols: Geological Society of America Bulletin, v. 105, no. 2, p. 129-136.

Marce, R., Martínez, E.N., Armengol, J., Caputo, L., and López, P., 2006, Elemental ratios in sediments as indicators of ecological processes in Spanish reservoirs: Limnetica, v. 25, no. 1, p. 499-512.

McInerney, F.A., and Wing, S.L., 2011, The Paleocene-Eocene Thermal Maximum: A perturbation of carbon cycle, climate, and biosphere with implications for the future: Annual Review of Earth and Planetary Sciences, v. 39, p. 489-516.

Moore, E.A., and Kurtz, A.C., 2008, Black carbon in Paleocene–Eocene boundary sediments: A test of biomass combustion as the PETM trigger: Palaeogeography, Palaeoclimatology, Palaeoecology, v. 267, no. 1, p. 147-152.

Mueller, E.R., and Pitlick, J., 2013, Sediment supply and channel morphology in mountain river systems: 1. Relative importance of lithology, topography, and climate: Journal of Geophysical Research: Earth Surface, v. 118, no. 4, p. 2325-2342.

Nordt, L., and Driese, S., 2010, New weathering index improves paleorainfall estimates from Vertisols: Geology, v. 38, no. 5, p. 407-410.

Panchuk, K., Ridgwell, A., and Kump, L., 2008, Sedimentary response to Paleocene-Eocene Thermal Maximum carbon release: A model-data comparison: Geology, v. 36, no. 4, p. 315-318.

Penman, D.E., Hönisch, B., Zeebe, R.E., Thomas, E., and Zachos, J.C., 2014, Rapid and sustained surface ocean acidification during the Paleocene-Eocene Thermal Maximum: Paleoceanography, v. 29, no. 5, p. 357-369.

Scheidegger, Y., Saurer, M., Bahn, M., and Siegwolf, R., 2000, Linking stable oxygen and carbon isotopes with stomatal conductance and photosynthetic capacity: a conceptual model: Oecologia, v. 125, no. 3, p. 350-357.

Schmitz, B., and Pujalte, V., 2007, Abrupt increase in seasonal extreme precipitation at the Paleocene-Eocene boundary: Geology, v. 35, no. 3, p. 215-218.

Secord, R., Wing, S.L., and Chew, A., 2008, Stable isotopes in early Eocene mammals as indicators of forest canopy structure and resource partitioning: Paleobiology, v. 34, no. 2, p. 282-300.

Self, J., Johnson, R., Brownfield, M., and Mercier, T., 2010, Stratigraphic cross sections of the Eocene Green River Formation in the Piceance Basin, northwestern Colorado: US Geological Survey Digital Data Series DDS-69-Y, p. 7.

Sewall, J.O., and Sloan, L.C., 2006, Come a little bit closer: A high-resolution climate study of the early Paleogene Laramide foreland: Geology, v. 34, no. 2, p. 81-84.

Sexton, P.F., Norris, R.D., Wilson, P.A., et al., 2011, Eocene global warming events driven by ventilation of oceanic dissolved organic carbon: Nature, v. 471, no. 7338, p. 349-352.

Sheldon, N.D., and Tabor, N.J., 2009, Quantitative paleoenvironmental and paleoclimatic reconstruction using paleosols: Earth-Science Reviews, v. 95, no. 1, p. 1-52.

Sluijs, A., Schouten, S., Donders, T.H., et al., 2009, Warm and wet conditions in the Arctic region during Eocene Thermal Maximum 2: Nature Geoscience, v. 2, no. 11, p. 777-780.

Sluijs, A., Schouten, S., Pagani, M., et al., 2006, Subtropical Arctic Ocean temperatures during the Palaeocene/Eocene thermal maximum: Nature, v. 441, no. 7093, p. 610-613.

Snell, K.E., Thrasher, B.L., Eiler, J.M., Koch, P.L., Sloan, L.C., and Tabor, N.J., 2013, Hot summers in the Bighorn Basin during the early Paleogene: Geology, v. 41, no. 1, p. 55-58.

Stap, L., Lourens, L.J., Thomas, E., Sluijs, A., Bohaty, S., and Zachos, J.C., 2010, High-resolution deep-sea carbon and oxygen isotope records of Eocene Thermal Maximum 2 and H2: Geology, v. 38, no. 7, p. 607-610.

Thomas, E., 2007, Cenozoic mass extinctions in the deep sea: What perturbs the largest habitat on Earth?: Geological Society of America Special Papers, v. 424, p. 1-23.

Thomas, E., 1989, Development of Cenozoic deep-sea benthic foraminiferal faunas in Antarctic waters: Geological Society, London, Special Publications, v. 47, no. 1, p. 283-296.

Weissmann, G., Hartley, A., Nichols, G., Scuderi, L., Olson, M., Buehler, H., and Banteah, R., 2010, Fluvial form in modern continental sedimentary basins: distributive fluvial systems: Geology, v. 38, no. 1, p. 39-42.

Weissmann, G., Hartley, A., Scuderi, L., et al., 2013, Prograding distributive fluvial systems: geomorphic models and ancient examples: New Frontiers in Paleopedology and Terrestrial Paleoclimatology: SEPM, Special Publication, v. 104, p. 131-147.

Westerhold, T., Röhl, U., McCarren, H.K., and Zachos, J.C., 2009, Latest on the absolute age of the Paleocene–Eocene Thermal Maximum (PETM): new insights from exact stratigraphic position of key ash layers 19 and– 17: Earth and Planetary Science Letters, v. 287, no. 3, p. 412-419.

Wing, S., Bloch, J., Bowen, G., et al., 2009, Coordinated sedimentary and biotic change during the Paleocene–Eocene Thermal Maximum in the Bighorn Basin, Wyoming, USA, in Climatic and Biotic Events of the Paleogene (CBEP 2009), extended abstracts from an international conference in Wellington, New Zealand, p. 15.

Zachos, J.C., Dickens, G.R., and Zeebe, R.E., 2008, An early Cenozoic perspective on greenhouse warming and carbon-cycle dynamics: Nature, v. 451, no. 7176, p. 279-283.

Zachos, J.C., Rohl, U., Schellenberg, S.A., et al., 2005, Rapid acidification of the ocean during the Paleocene-Eocene thermal maximum: Science (New York, N.Y.), v. 308, no. 5728, p. 1611-1615.

Zachos, J.C., Shackleton, N.J., Revenaugh, J.S., Palike, H., and Flower, B.P., 2001, Climate response to orbital forcing across the Oligocene-Miocene boundary: Science (New York, N.Y.), v. 292, no. 5515, p. 274-278.

Zeebe, R.E., Zachos, J.C., and Dickens, G.R., 2009, Carbon dioxide forcing alone insufficient to explain Palaeocene "Eocene Thermal Maximum warming: Nature Geoscience, v. 2, no. 8, p. 576-580.

Appendix 1: Tables

Table 1: All δ¹³C and δ¹⁸O from the Piceance Basin

Sample ID	Stratigraphic Height (m)	δ13C	δ18O
PICN1501	2.00	-11.00	-5.44
PICN1501	2.00	-10.85	-5.12
PICN1501	2.00	-10.92	-5.19
PICN1502	4.85		-6.27
PICN1502	4.85		-5.59
PICN1503	5.05	-10.88	-5.53
PICN1503	5.05	-10.97	-5.07
PICN1503	5.05	-10.88	-5.19
PICN1504	5.90	-11.49	-5.05
PICN1505	8.08	-11.82	-6.32
PICN1505	8.08	-11.98	-6.66
PICN1505	8.08		-6.47
PICN1506	10.88		-6.00
PICN1506	10.88	-11.25	-6.05
PICN1506	10.88	-11.07	-5.92
PICN1508	15.28	-10.58	-6.48
PICN1508	15.28	-10.98	
PICN1508	15.28		-6.38
PICN1510	19.78	-11.12	-6.05
PICN1510	19.78		-6.42
PICN1510	19.78	-11.27	-6.25
PICN1511	22.43	-11.52	-6.25
PICN1511	22.43	-11.19	-6.13
PICN1511	22.43	-11.14	-6.03
PICN1513	27.46	-13.05	-6.94
PICN1513	27.46	-13.37	-7.14
PICN1513	27.46		-7.43
PICN1514	30.11	-10.28	-5.57
PICN1514	30.11	-10.02	-5.54
PICN1514	30.11		-5.96
PICN1515	31.46	-10.20	-5.68
PICN1515	31.46	-10.25	-5.49
PICN1515	31.46	-10.38	-5.86
PICN1516	37.84	-11.98	-6.26
PICN1516	37.84	-11.63	-6.65
PICN1517	44.74	-12.33	-7.02

PICN1517	44.74	-12.28	-7.17
PICN1517	44.74	-12.18	-6.62
PICN1518	44.94	-12.41	-7.26
PICN1518	44.94	-12.14	-7.03
PICN1518	44.94	-12.01	-7.03
PICN1519	45.89	-12.05	
PICN1519	45.89	-11.66	
PICN1519	45.89	-11.75	
PICN1520	46.64	-12.38	-6.82
PICN1520	46.64	-12.06	-7.01
PICN1520	46.64	-12.28	-6.56
PICN1521	47.74		-6.45
PICN1521	47.74	-11.10	
PICN1521	47.74		-6.23
PICN1522	48.84		-6.86
PICN1522	48.84	-12.07	-7.27
PICN1522	48.84	-11.98	-6.82
PICN1527	52.35	-12.87	-6.09
PICN1527	52.35	-13.15	-6.26
PICN1527	52.35		-6.03
PICN1526	52.50	-12.77	
PICN1526	52.50	-13.00	-6.78
PICN1526	52.50	-13.26	-6.66
PICN1528	53.10	-13.43	-6.10
PICN1528	53.10	-13.30	-6.05
PICN1528	53.10	-13.31	-5.84
PICN1529	54.35	-14.16	-5.81
PICN1529	54.35	-14.12	-5.64
PICN1530	55.93	-14.23	-6.45
PICN1530	55.93	-14.00	-6.08
PICN1530	55.93	-14.07	
PICN1531	56.88	-13.44	-5.99
PICN1531	56.88	-13.29	-5.53
PICN1531	56.88	-13.13	-5.66
PICN1532	59.20	-12.92	-6.58
PICN1532	59.20		-6.88
PICN1532	59.20	-12.89	-6.42
PICN1533	60.25	-12.82	-6.35
PICN1533	60.25	-12.86	-6.24
PICN1533	60.25	-12.80	
PICN1534	60.78	-13.11	-6.20
PICN1534	60.78	-13.09	-6.10
PICN1534	60.78	-12.93	-6.02

PICN1535	62.43		-7.62
PICN1535	62.43	-12.61	-7.58
PICN1535	62.43	-12.61	
PICN6373	63.73	-12.52	-6.75
PICN6373	63.73	-12.31	-7.15
PICN6393	63.93	-12.89	-6.38
PICN6393	63.93	-12.84	-6.53
PICN6568	65.68	-12.04	-6.92
PICN6568	65.68	-11.92	-7.12
PICN1536	66.18	-11.67	-7.01
PICN1536	66.18	-11.58	-7.05
PICN1536	66.18	-11.66	-7.02
PICN1537	67.04	-11.62	-7.03
PICN1537	67.04	-11.68	-7.02
PICN1537	67.04	-11.46	-7.19
PICN1538	67.57	-11.72	-7.57
PICN1538	67.57	-11.33	-7.60
PICN1538	67.57	-11.67	-7.79
PICN1539	68.33	-11.77	-7.20
PICN1539	68.33	-12.13	-7.25
PICN1539	68.33	-11.83	-6.94
PICN1540	69.22	-11.95	-7.15
PICN1540	69.22	-11.95	-7.13
PICN1540	69.22	-12.04	-7.04
PICN1541	70.46	-12.44	-6.96
PICN1541	70.46	-11.93	-7.32
PICN1541	70.46	-12.09	-6.93
PICN1542	71.36	-12.07	-7.02
PICN1542	71.36	-12.57	-7.13
PICN1542	71.36	-12.47	-6.93
PICN1544	75.39	-12.32	-5.68
PICN1544	75.39	-12.02	-5.87
PICN1544	75.39	-12.36	-5.65
PICN7669	76.69	-11.48	-7.03
PICN7669	76.69	-11.44	-6.84
PICN1545	77.48	-11.33	-6.88
PICN1545	77.48	-11.26	-7.15
PICN1545	77.48	-11.17	-7.08
PICN1546	83.21	-11.89	-6.92
PICN1546	83.21	-11.80	-7.27
PICN1546	83.21	-11.76	-7.11
PICN1547	84.26		-6.21
PICN1547	84.26		-6.08

PICN1548	84.61	-11.56	-5.99
PICN1548	84.61	-11.62	-6.06
PICN1548	84.61	-11.46	-6.07
PICN1549	85.23	-11.59	-6.05
PICN1549	85.23	-11.71	-6.20
PICN1549	85.23	-11.67	-5.82
PICN1550	86.38	-11.76	
PICN1550	86.38	-12.15	-5.76
PICN1550	86.38	-12.11	-5.81
PICN1551	87.38	-11.85	-5.81
PICN1551	87.38	-11.82	-5.91
PICN1551	87.38	-11.20	
PICN1552	90.68	-10.88	
PICN1552	90.68	-11.29	
PICN1552.5	91.00		-6.06
PICN1552.5	91.00		-6.17
PICN1553	91.73	-10.09	-6.69
PICN1553	91.73	-10.30	-6.45
PICN1553	91.73	-10.58	-6.40
PICNB1	118.01	-11.90	
PICNB2	124.01	-12.00	
PICNB3	129.01	-11.60	
PICNB4	133.01	-10.80	

Table 1

All δ^{13}C and δ^{18}O of carbonate nodules from the Piceance Basin are presented in Table 1. δ^{13}C and δ^{18}O values that were not within .5 ‰ of other nodules from the same stratigraphic height were removed. All data highlighted purple are background, all data highlighted in orange are CIE onset, all data highlighted in red are CIE peak and all data highlighted in blue are CIE return. Nodules 1522 – 1524 are ETM2 and nodules 1536 – 1535 are H2.

Table 2: Al/Si and CALMAG data from Piceance Basin

Sample ID	Stratigraphic Height (m)	Al/Si	CALMAG
1501D	2	0.332	90.239
1502D	4.85	0.236	80.801
1503D	5.05	0.237	83.961
1508D	15.28	0.307	85.875
1509D	16.78	0.270	88.484
1510D	19.78	0.216	84.939
1511D	22.43	0.255	87.919
1513D	27.46	0.357	90.281
1514D	30.11	0.284	88.071
1515D	31.46	0.212	88.305
1516D	37.84	0.231	84.100
1517D	44.74	0.263	87.578
1518D	44.94	0.210	85.061
1519D	45.89	0.182	82.318
1520D	46.64	0.192	84.374
1521D	47.74	0.165	87.015
1522D	48.84	0.317	88.170
1523D	49.62	0.224	77.916
1524D	50.77	0.136	89.086
1525D	52.15	0.292	88.248
1527D	52.35	0.287	88.728
1526D	52.5	0.304	88.523
1528D	53.1	0.301	86.122
1529D	54.35	0.306	81.258
1530D	55.93	0.305	84.225
1531D	56.88	0.314	85.207
1532D	59.2	0.320	85.054
1533D	60.25	0.237	74.705
1534D	60.78	0.324	87.152
6373D	63.73	0.305	86.500
6393D	63.93	0.306	87.909
1536D	66.18	0.221	83.055
1537D	67.04	0.232	84.907
1538D	67.57	0.189	63.536
1539D	68.33	0.246	85.123
1540D	69.22	0.279	83.860
1541D	70.46	0.326	88.224
1542D	71.36	0.306	82.947
1543D	74.78	0.238	52.951

1544D	75.39	0.322	77.256
7669D	76.69	0.274	90.860
1545D	77.48	0.287	90.428
1546D	83.21	0.209	79.962
1547D	84.26	0.257	90.553
1548D	84.61	0.245	88.119
1549D	85.23	0.237	82.145
1550D	86.38	0.278	87.570
1551D	87.38	0.242	84.900
1552D	90.68	0.301	89.931
1553D	91.73	0.263	63.372

Table 2

Al/Si and CALMAG paleosol data from the Piceance Basin are presented in Table 2. CALMAG values below 80 are highlighted in red and dropped from the dataset as they are indicative of paleosols that aren't fully formed/weathered. All data highlighted purple are background, all data highlighted in orange are CIE onset, all data highlighted in red are CIE peak and all data highlighted in blue are CIE return. Nodules 1522 – 1524 are ETM2 and nodules 1536 – 1535 are H2.

Table 3: Ca/Al, K/Al, Mg/Al and Σbase/Al data from Piceance Basin

Sample ID	Stratigraphic Height (m)	Σbase/Al	Ca/Al	K/Al	Mg/Al
1501D	2	0.258	0.013	0.150	0.096
1502D	4.85	0.400	0.079	0.163	0.158
1503D	5.05	0.354	0.040	0.163	0.151
1508D	15.28	0.320	0.016	0.156	0.149
1509D	16.78	0.304	0.017	0.174	0.113
1510D	19.78	0.332	0.038	0.155	0.140
1511D	22.43	0.287	0.020	0.149	0.117
1513D	27.46	0.239	0.023	0.131	0.085
1514D	30.11	0.294	0.027	0.159	0.108
1515D	31.46	0.287	0.030	0.154	0.102
1516D	37.84	0.342	0.031	0.153	0.158
1517D	44.74	0.286	0.034	0.144	0.107
1518D	44.94	0.319	0.062	0.143	0.113
1519D	45.89	0.362	0.098	0.147	0.117
1520D	46.64	0.333	0.052	0.148	0.133
1521D	47.74	0.295	0.070	0.146	0.079
1522D	48.84	0.277	0.013	0.143	0.121
1523D	49.62	0.430	0.169	0.147	0.114
1524D	50.77	0.280	0.031	0.157	0.091
1525D	52.15	0.278	0.023	0.145	0.110
1527D	52.35	0.274	0.015	0.147	0.112
1526D	52.5	0.266	0.021	0.137	0.109
1528D	53.1	0.302	0.026	0.141	0.135
1529D	54.35	0.383	0.069	0.152	0.162
1530D	55.93	0.346	0.040	0.158	0.147
1531D	56.88	0.322	0.055	0.149	0.118
1532D	59.2	0.314	0.032	0.139	0.144
1533D	60.25	0.485	0.193	0.146	0.146
1534D	60.78	0.301	0.022	0.153	0.125
6373D	63.73	0.292	0.025	0.136	0.131
6393D	63.93	0.278	0.015	0.141	0.123
1536D	66.18	0.350	0.029	0.146	0.175
1537D	67.04	0.336	0.026	0.158	0.152
1538D	67.57	0.730	0.451	0.156	0.123
1539D	68.33	0.330	0.041	0.156	0.133
1540D	69.22	0.345	0.063	0.153	0.129
1541D	70.46	0.268	0.010	0.134	0.123

1542D	71.36	0.358	0.046	0.153	0.160
1543D	74.78	1.041	0.727	0.153	0.162
1544D	75.39	0.444	0.142	0.149	0.152
7669D	76.69	0.269	0.007	0.169	0.093
1545D	77.48	0.267	0.012	0.161	0.094
1546D	83.21	0.385	0.139	0.134	0.112
1547D	84.26	0.236	0.017	0.132	0.087
1548D	84.61	0.297	0.024	0.162	0.111
1549D	85.23	0.367	0.115	0.149	0.102
1550D	86.38	0.283	0.030	0.141	0.112
1551D	87.38	0.332	0.063	0.155	0.115
1552D	90.68	0.235	0.021	0.123	0.091
1553D	91.73	0.724	0.462	0.146	0.116

Table 3

Ca/Al, K/Al, Mg/Al and Σbase/Al [(Ca+Mg+K)/Al] paleosol data from the Piceance Basin are presented in Table 3. All data highlighted purple are background, all data highlighted in orange are CIE onset, all data highlighted in red are CIE peak and all data highlighted in blue are CIE return. Nodules 1522 – 1524 are ETM2 and nodules 1536 – 1535 are H2.

Table 4: Mn and Fe data from Piceance Basin

Sample ID	Stratigraphic Height (m)	Mn	Fe
1501D	2	0.022	8.243
1502D	4.85	0.076	5.878
1503D	5.05	0.039	7.323
1508D	15.28	0.034	9.937
1509D	16.78	0.021	7.139
1510D	19.78	0.038	4.895
1511D	22.43	0.034	6.507
1513D	27.46	0.033	10.738
1514D	30.11	0.023	7.432
1515D	31.46	0.020	3.886
1516D	37.84	0.033	0.618
1517D	44.74	0.031	7.075
1518D	44.94	0.034	4.644
1519D	45.89	0.048	4.399
1520D	46.64	0.032	4.885
1521D	47.74	0.055	3.350
1522D	48.84	0.019	6.986
1523D	49.62	0.240	4.650
1524D	50.77	0.026	2.874
1525D	52.15	0.023	6.751
1527D	52.35	0.023	7.121
1526D	52.5	0.024	7.416
1528D	53.1	0.024	7.422
1529D	54.35	0.035	7.024
1530D	55.93	0.031	6.666
1531D	56.88	0.027	7.539
1532D	59.2	0.030	7.596
1533D	60.25	0.061	5.069
1534D	60.78	0.033	7.213
6373D	63.73	0.030	7.475
6393D	63.93	0.021	6.855
1536D	66.18	0.029	4.618
1537D	67.04	0.030	5.474
1538D	67.57	0.263	4.085
1539D	68.33	0.041	6.120

1540D	69.22	0.039	6.825
1541D	70.46	0.024	7.939
1542D	71.36	0.034	7.222
1543D	74.78	0.182	3.634
1544D	75.39	0.057	7.545
7669D	76.69	0.025	7.009
1545D	77.48	0.019	6.006
1546D	83.21	0.057	4.202
1547D	84.26	0.021	6.281
1548D	84.61	0.025	5.103
1549D	85.23	0.054	5.681
1550D	86.38	0.036	6.813
1551D	87.38	0.033	5.557
1552D	90.68	0.042	8.038
1553D	91.73	0.299	5.668

Table 4

Mn and Fe paleosol data from the Piceance Basin are presented in Table 4. All data highlighted purple are background, all data highlighted in orange are CIE onset, all data highlighted in red are CIE peak and all data highlighted in blue are CIE return. Nodules 1522 – 1524 are ETM2 and nodules 1536 – 1535 are H2.